

Myocardial Motion Estimation from Medical Images Using the Monogenic Signal

Martino Alessandrini, Adrian Basarab, Hervé Liebgott, and Olivier Bernard

Abstract—We present a method for the analysis of heart motion from medical images. The algorithm exploits monogenic signal theory, recently introduced as an N-dimensional generalization of the analytic signal. The displacement is computed locally by assuming the conservation of the monogenic phase over time. A local affine displacement model is considered to account for typical heart motions as contraction/expansion and shear. A coarse-to-fine B-spline scheme allows a robust and effective computation of the model's parameters, and a pyramidal refinement scheme helps to handle large motions. Robustness against noise is increased by replacing the standard point-wise computation of the monogenic orientation with a robust least-squares orientation estimate. Given its general formulation, the algorithm is well suited for images from different modalities, in particular for those cases where time variant changes of local intensity invalidate the standard brightness constancy assumption. This paper evaluates the method's feasibility on two emblematic cases: cardiac tagged magnetic resonance and cardiac ultrasound. In order to quantify the performance of the proposed method, we made use of realistic synthetic sequences from both modalities for which the benchmark motion is known. A comparison is presented with state-of-the-art methods for cardiac motion analysis. On the data considered, these conventional approaches are outperformed by the proposed algorithm. A recent global optical-flow estimation algorithm based on the monogenic curvature tensor is also considered in the comparison. With respect to the latter, the proposed framework provides, along with higher accuracy, superior robustness to noise and a considerably shorter computation time.

Index Terms—Cardiac ultrasound, illumination changes, iterative refinement, monogenic signal, optical flow, optimal window size, tagged-magnetic resonance imaging (tMRI).

I. INTRODUCTION

THE MONOGENIC signal has been recently introduced by Felsberg [1] as an extension of the analytic signal concept to multiple dimensions. Like the latter, the monogenic signal provides the *local amplitude* and *local phase* signal features. Additionally, it also contains information on the *local orientation*. These three local features are pointwise

Manuscript received March 26, 2012; revised October 17, 2012; accepted October 17, 2012. This work was supported in part by the Agence Nationale de la Recherche under the US-Tagging Grant. The associate editor coordinating the review of this manuscript and approving it for publication was Prof. Richard J. Radke.

M. Alessandrini, H. Liebgott, and O. Bernard are with the Université de Lyon, CREATIS, CNRS UMR5220, Inserm U1044, INSA-Lyon, Université Lyon 1, Lyon 69622, France (e-mail: martino.alessandrini@creatis.insa-lyon.fr; liebgott@creatis.univ-lyon1.fr; olivier.bernard@creatis.insa-lyon.fr).

A. Basarab is with the Institut de Recherche en Informatique de Toulouse, Toulouse CNRS UMR5505, France (e-mail: adrian.basarab@irit.fr).

Color versions of one or more of the figures in this paper are available online at <http://ieeexplore.ieee.org>.

Digital Object Identifier 10.1109/TIP.2012.2226903

orthogonal, which means that they represent independent information: the local amplitude represents the local intensity or dynamics, the local phase describes the local symmetry or grey value transition, and the local orientation describes the direction of the highest signal variance. Decoupling the local energy from the image structure, accounted for by phase and orientation, has made it possible to derive effective solutions to a number of image-processing problems, in particular when the more traditional pixel intensity cannot be considered as a reliable feature.

This situation is often encountered in medical imaging. In cardiac ultrasound, the local brightness varies over time due to the changes in the angle between the myocardial fibers and the direction of propagation of the acoustic beam or due to out-of-plane motions [2]. In magnetic resonance imaging (MRI), intensity variations stem from magnetic field inhomogeneities and scanner-related intensity artifacts [3]. In tagged-MRI (tMRI) [4], tags fade exponentially over time depending on the T1 relaxation time [5], [6]. Obviously, the same problems are encountered when contrast agents are used, such as in perfusion MRI [7] or when registration of images from different modalities, such as computed tomography (CT) and positron emission tomography (PET), is needed [8], [9].

These considerations explain the rapidly growing interest in monogenic signal analysis applied to medical imaging problems over the last few years. For example, one could cite successful applications of monogenic analysis in boundary detection [10], [11], segmentation [12], multi-modal registration [8], [9], ultrasound image compounding [13], multi-view image registration [14], wavelet filtering [15] and envelope detection [16].

In this context, the algorithm presented in this paper, addresses a further fundamental problem in the field of medical imaging, *i.e.* the estimation of myocardial motion. Assessment of myocardial elasticity and contractility is indeed essential in clinical practice to evaluate the degree of ischemia and infarction as well as for surgical planning [17], [18].

We compute the displacement estimate locally by assuming the conservation of the monogenic phase in lieu of traditional pixel brightness. The general formulation takes inspiration from the work of Felsberg in [19]; nevertheless, the novelties with respect to this study are manifold and substantial:

- 1) Locally, the size of the image window is selected in order to have the most consistent motion estimate. This operation is fully automatic and computationally effective because of an adaptation of the B-spline multiresolution approach for the image moments computation proposed by Sühling *et al.* in [20], [21]. By doing

so, a common source of error in local techniques, related to an inadequate choice of the window size, is avoided.

- 2) Felsberg's pure translation model is replaced with an affine model. The affine model, a part of translation, can account for rotation, expansion, compression and shear, and provides a realistic description of the motion patterns typical of the cardiac muscle [17]. Furthermore, as the first-order spatial derivatives of the displacement are also computed, it allows the direct computation of the cardiac strain, with no need for numerical differencing [18].
- 3) The robustness to noise is improved by employing a least squares estimate of the monogenic orientation in place of the standard point-wise estimate [22].
- 4) An incremental *coarse-to-fine* pyramidal scheme is used to refine the precision of the final estimate.

The general formulation makes the algorithm well suited for images from different modalities. In particular, this paper evaluates its performance on tagged magnetic resonance imaging (tMRI) [4] and cardiac ultrasound image sequences. In order to quantify performance, we made use of realistic synthetic sequences for both modalities, for which the benchmark motion was known. In each experiment, a comparison is presented with state-of-the-art methods in the related field. They include SinMod [23] for tMRI images and the Sühling [21] and Felsberg [19] algorithms for ultrasound. In both cases, the recent algorithm reported in Zang *et al.* [24] is also considered in the comparison. Indeed, due to the monogenic signal formulation at its base, it can be considered a possible competitor to the algorithm proposed herein.

The paper proceeds as follows. In Section II the monogenic signal theory is briefly summarized and the robust computation of the orientation is introduced. In Section III the proposed optical flow estimation algorithm is described. Section IV discusses some implementation details. In Section V the problem of cardiac motion analysis from tMRI and cardiac ultrasound is briefly summarized and the results are presented. Concluding remarks are left to Section VI.

II. MONOGENIC SIGNAL COMPUTATION

The most practical aspects of the monogenic signal computation will be reviewed here. For further details, we address the interested reader to [1], [25] and to [22] for a more intuitive derivation.

The monogenic signal provides an extension of the standard analytic signal for multidimensional data. Although the theory is valid for a general number N of dimensions ($N > 1$), we consider here the case at hand of 2D grayscale images $I: \Omega \rightarrow \mathbb{R}, \Omega \subset \mathbb{R}^2$.

The image model adopted in phase-based processing is [19], [26]

$$I(\mathbf{x}) = A(\mathbf{x}) \cos(\varphi(\mathbf{x})) \quad (1)$$

where $\mathbf{x} = [x, y]$ is the spatial coordinate vector, $A(\mathbf{x})$ is the *local amplitude* and $\varphi(\mathbf{x})$ is the *local phase*. Additionally, monogenic signal theory assumes a local intrinsic dimensionality one [19], [26], *i.e.*, the local variations of I are

concentrated along a single direction, defined by the *local orientation* $\theta(\mathbf{x})$.

The monogenic signal computes the image features of amplitude, phase and orientation from the responses to three 2D spherical quadrature filters (SQFs) [1]. The SQFs consist of one *even* rotation invariant bandpass $b_e(\mathbf{x}; \lambda_0)$ filter and two *odd* bandpass filters $b_{o1}(\mathbf{x}; \lambda_0)$ and $b_{o2}(\mathbf{x}; \lambda_0)$, where λ_0 is the filter wavelength, defined as the reciprocal of the normalized center frequency f_0 . Note that in the following the dependency of the filter responses on the center frequency will be omitted for the sake of simplicity. The odd filters are computed from the Riesz transform of the even filter [1], [19]. In the frequency domain it is

$$B_{o1}(\boldsymbol{\omega}) = -\frac{j\omega_x}{|\boldsymbol{\omega}|} \cdot B_e(\boldsymbol{\omega}), \quad B_{o2}(\boldsymbol{\omega}) = -\frac{j\omega_y}{|\boldsymbol{\omega}|} \cdot B_e(\boldsymbol{\omega}) \quad (2)$$

where capital letters denote the Fourier transformed quantities and $\boldsymbol{\omega} = [\omega_x, \omega_y]^T$ is the normalized angular frequency. Several SQF families have been employed in the literature: a comparison of the most popular ones is presented in [27]. A similar study is beyond the scope of this paper. Here, as recommended in [25], [28], the difference of Poisson (DoP) kernel is adopted:

$$B_e(\boldsymbol{\omega}) = \exp(-|\boldsymbol{\omega}|s_1) - \exp(-|\boldsymbol{\omega}|s_2) \quad (3)$$

where $|\boldsymbol{\omega}|$ is the normalized angular frequency and s_1 and $s_2 > s_1$ are two scale parameters. It can be shown that the wavelength is related to the two scales by:

$$\lambda_0 = 2\pi \frac{s_1 - s_2}{\log(s_1) - \log(s_2)}. \quad (4)$$

From the three filter responses, monogenic phase $\varphi(\mathbf{x})$, orientation $\theta(\mathbf{x})$ and amplitude $A(\mathbf{x})$ of I are obtained as:

$$\begin{aligned} \theta(\mathbf{x}) &= \arctan\left(\frac{q_2(\mathbf{x})}{q_1(\mathbf{x})}\right) \\ \varphi(\mathbf{x}) &= \arctan\left(\frac{|\mathbf{q}(\mathbf{x})|}{p(\mathbf{x})}\right) \\ A(\mathbf{x}) &= \sqrt{p^2(\mathbf{x}) + |\mathbf{q}(\mathbf{x})|^2} \end{aligned} \quad (5)$$

where $p(\mathbf{x}) = (I * b_e)(\mathbf{x})$, $q_1(\mathbf{x}) = (I * b_{o1})(\mathbf{x})$, $q_2(\mathbf{x}) = (I * b_{o2})(\mathbf{x})$, $\mathbf{q}(\mathbf{x}) = [q_1(\mathbf{x}), q_2(\mathbf{x})]^T$ and “*” denotes 2D convolution.

From the filter responses, the *local frequency* feature, defined as the derivative of the phase along \mathbf{n} , can also be computed as [19]:

$$f \triangleq (\nabla\varphi)^T \cdot \mathbf{n} = \frac{p\nabla^T \mathbf{q} - \mathbf{q}^T \nabla p}{p^2 + |\mathbf{q}|^2} \quad (6)$$

where $\nabla = [\partial_x, \partial_y]^T$. Dependency on \mathbf{x} is implied.

Monogenic phase and orientation can be conveniently combined in the *phase vector* $\mathbf{r}(\mathbf{x}) = [r_1(\mathbf{x}), r_2(\mathbf{x})] = \varphi(\mathbf{x}) \cdot \mathbf{n}(\mathbf{x})$, with $\mathbf{n}(\mathbf{x}) = [\cos(\theta(\mathbf{x})), \sin(\theta(\mathbf{x}))]^T$ [1], [19]. The dependency on \mathbf{x} of all the aforementioned features will be omitted in the sequel unless necessary.

A. Robust Orientation Computation

In order to improve the robustness against image noise, in this study we replace the classical point-wise estimate of θ (5), with a robust least-squares estimate, inspired by the structure tensor formalism [29]. The scheme presented was proposed by Unser *et al.* in [22].

The least-squares orientation estimate is obtained by maximizing the directional Hilbert transform $\mathcal{H}_\theta I(\mathbf{x})$ averaged over a local neighborhood v_σ

$$\bar{\theta}(\mathbf{x}) = \arg \max_{\theta' \in [-\pi, \pi]} \int_{\mathbb{R}^2} v_\sigma(\mathbf{x}' - \mathbf{x}) \cdot |\mathcal{H}_{\theta'} I(\mathbf{x}')|^2 d\mathbf{x}' \quad (7)$$

where v_σ corresponds here to a Gaussian kernel with variance σ^2 and the directional Hilbert transform is defined in the frequency domain as

$$\mathcal{H}_\theta(\boldsymbol{\omega}) = \frac{\omega_x \cos(\theta) + \omega_y \sin(\theta)}{|\boldsymbol{\omega}|}. \quad (8)$$

It is shown in [22] that (7) corresponds to the classical solution (5) if $v_\sigma(\mathbf{x}) = \delta(\mathbf{x})$. The maximization problem (7) is solved by the eigenvector associated with the largest eigenvalue of the 2×2 matrix $\mathbf{T}(\mathbf{x})$, with entries

$$[\mathbf{T}(\mathbf{x})]_{nm} = \int_{\mathbb{R}^2} v_\sigma(\mathbf{x}' - \mathbf{x}) q_n(\mathbf{x}') q_m(\mathbf{x}') d\mathbf{x}' \quad (9)$$

with $n, m = \{1, 2\}$. The matrix \mathbf{T} can be assimilated to a Riesz-transform counterpart of the standard structure tensor. The new estimate is then given by

$$\bar{\theta}(\mathbf{x}) = \frac{1}{2} \arctan \left(\frac{2[\mathbf{T}(\mathbf{x})]_{12}}{[\mathbf{T}(\mathbf{x})]_{22} - [\mathbf{T}(\mathbf{x})]_{11}} \right). \quad (10)$$

Due to the averaging operation in (7), this alternative estimate is expected to be less sensitive to image noise than the traditional estimate. An example of this property is given in Fig. 1. We conclude this section by noting that this different orientation definition also affects the monogenic phase computation. In particular, the $|\mathbf{q}|$ term appearing in the second equation of (5) must now be replaced with $s(\mathbf{x}) = q_1 \cos \bar{\theta} + q_2 \sin \bar{\theta}$.

III. MULTISCALE OPTICAL FLOW COMPUTATION FROM THE MONOGENIC PHASE

As in [19], the displacement field $\mathbf{d}(\mathbf{x}) = [d_1(\mathbf{x}), d_2(\mathbf{x})]^T$ along x and y between two frames is estimated by replacing the traditional brightness constancy assumption with the more robust *monogenic phase constancy assumption*. This is conveniently expressed in terms of the monogenic phase vector as $\mathbf{r}(\mathbf{x}, t+1) = \mathbf{r}(\mathbf{x} - \mathbf{d}(\mathbf{x}), t)$. Assuming small displacements, the first-order Taylor expansion can be used $\mathbf{r}(\mathbf{x} - \mathbf{d}(\mathbf{x}), t) \approx \mathbf{r}(\mathbf{x}, t) - \mathbf{J}(\mathbf{x}, t) \cdot \mathbf{d}(\mathbf{x})$, where \mathbf{J} is the Jacobian matrix of \mathbf{r} . Then, assuming all points translate of the same quantity \mathbf{d}_0 within a local window w centered in $\mathbf{x}_0 = [x_0, y_0]$, the following linear system of equations is obtained:

$$\begin{aligned} \langle \mathbf{J} \rangle_w \mathbf{d}_0 &= - \langle \mathbf{r}_t \rangle_w, \\ \mathbf{J}(\mathbf{x}, t) &= \begin{bmatrix} r_{1x}(\mathbf{x}, t) & r_{1y}(\mathbf{x}, t) \\ r_{2x}(\mathbf{x}, t) & r_{2y}(\mathbf{x}, t) \end{bmatrix} \end{aligned} \quad (11)$$

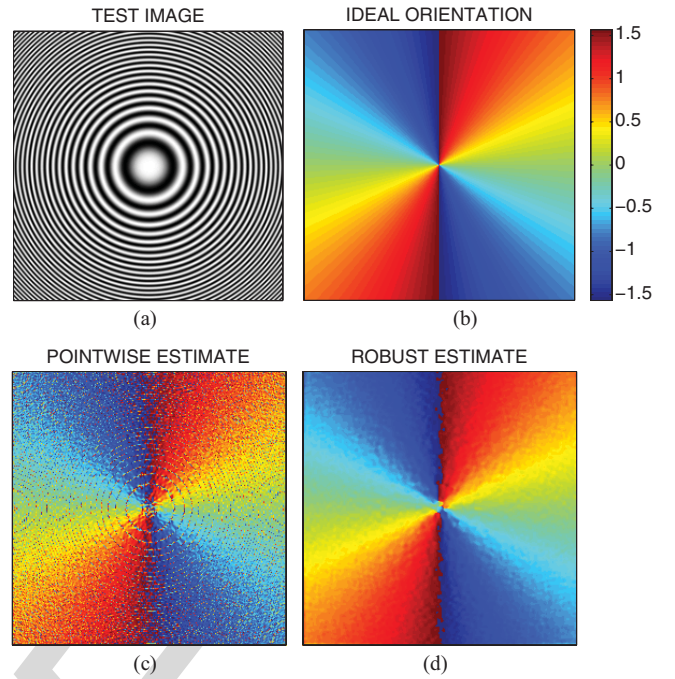


Fig. 1. Monogenic orientation estimate in the presence of noise. (a) Noise-free test image containing a full 360-degree range of orientations. (b) Ideal orientation. (c) and (d) Pointwise and robust ($\sigma = 2$) estimates in the presence of image noise (20 dB). Mean square error of the estimate is $1.2\text{E-}2$ for (c) and $2.7\text{E-}4$ for (d). Phases are wrapped in the $[-\pi/2, \pi/2]$ interval.

where $\mathbf{r}_t(\mathbf{x}, t) = [r_{1t}(\mathbf{x}, t), r_{2t}(\mathbf{x}, t)]$ denotes the time derivative of \mathbf{r} , approximated as $\mathbf{r}(\mathbf{x}, t+1) - \mathbf{r}(\mathbf{x}, t)$, $\langle \mathbf{v} \rangle_w$ denotes the weighted average $\int_{\Omega} w(\mathbf{x} - \mathbf{x}_0) \mathbf{v}(\mathbf{x}) d\mathbf{x}$ and $r_{ik} = \partial_k r_i$. Dependency on (\mathbf{x}, t) will be omitted in the following.

Assuming a 1D structure [19], \mathbf{J} must have rank one. It can be shown that its only eigenvalue corresponds to the monogenic frequency f in (6) while the associated eigenvector is $\mathbf{n} = [\cos(\theta), \sin(\theta)]^T$ [19], [22], this leads to the expression [19], [22]

$$\mathbf{J} = f \mathbf{n} \mathbf{n}^T = f \begin{bmatrix} \cos^2(\theta) & \sin(\theta) \cos(\theta) \\ \sin(\theta) \cos(\theta) & \sin^2(\theta) \end{bmatrix}. \quad (12)$$

The term \mathbf{r}_t is computed from the SQFs responses as [19]:

$$\mathbf{r}_t = \frac{p_t \mathbf{q}_{t+1} - \mathbf{q}_t p_{t+1}}{|p_t \mathbf{q}_{t+1} - \mathbf{q}_t p_{t+1}|} \arctan \left(\frac{|p_t \mathbf{q}_{t+1} - \mathbf{q}_t p_{t+1}|}{p_t p_{t+1} + \mathbf{q}_t^T \mathbf{q}_{t+1}} \right) \quad (13)$$

where subscripts “ t ” and “ $t+1$ ” denote the time instant.

We conclude by noting that (11) represents the monogenic phase counterpart of the popular Lucas & Kanade algorithm [30], where the matrix \mathbf{J} replaces the image structure tensor.

A. Affine Model

Clearly, the simple translation model employed by Felsberg is too restrictive in a general context. Also, its validity is heavily dependent on the choice of the size of w . The solution we propose is to replace the constant motion assumption with a more general model, such as the affine model [31], [32]. A part of translations, this accounts for rotation, expansion, compression and shear. In the context of this paper, the affine

259 model is of major interest because it provides a realistic
 260 description of the motion patterns of the cardiac muscle [17].
 261 A further relevant point is that, as the first-order spatial deriv-
 262 atives of the displacement are also computed, the Lagrangian
 263 strain tensor can be directly obtained from the latter, with no
 264 need for further numerical differencing. The local analysis of
 265 cardiac contractility is indeed fundamental in the diagnosis of
 266 pathological situations such as ischemia [18], [33].

267 Considering for simplicity a window w centered at
 268 $(x_0, y_0) = (0, 0)$, the affine model is written:

$$269 \quad \mathbf{d}(\mathbf{x}) = \mathbf{A}(\mathbf{x})\mathbf{u}, \quad \mathbf{A} = \begin{bmatrix} 1 & 0 & x & y & 0 & 0 \\ 0 & 1 & 0 & 0 & x & y \end{bmatrix} \quad (14)$$

270 where $\mathbf{u} = [d_{10}, d_{20}, d_{1x}, d_{1y}, d_{2x}, d_{2y}]^T$ is the new unknown
 271 vector: d_{10} and d_{20} correspond to the translation of the window
 272 center and $d_{ik} = \partial_k d_i$.

273 Plugging (14) into (11) leads to an underdetermined system
 274 of equations. The solution is obtained by pre-multiplying both
 275 terms by \mathbf{A}^T , hence

$$276 \quad \langle \mathbf{M} \rangle_w \mathbf{u} = \langle \mathbf{b} \rangle_w, \quad \mathbf{M} = \mathbf{A}^T \mathbf{J} \mathbf{A}, \quad \mathbf{b} = -\mathbf{A}^T \mathbf{r}_t. \quad (15)$$

277 Equation (15) represents the proposed monogenic phase
 278 version of the Lucas & Kanade algorithm with affine param-
 279 etrization of the displacement [21].

280 It can be shown that the entries of \mathbf{M} and \mathbf{b} are the local
 281 moments of orders zero to two of the spatial and temporal
 282 derivatives of r_1 and r_2 :

$$283 \quad \mathbf{M} = \begin{bmatrix} r_{1x} & r_{1y} & xr_{1x} & yr_{1x} & xr_{1y} & yr_{1y} \\ r_{2x} & r_{2y} & xr_{2x} & yr_{2x} & xr_{2y} & yr_{2y} \\ xr_{1x} & xr_{1y} & x^2r_{1x} & xyr_{1x} & x^2r_{1y} & xyr_{1y} \\ yr_{1x} & yr_{1y} & xyr_{1x} & y^2r_{1x} & xyr_{1y} & y^2r_{1y} \\ xr_{2x} & xr_{2y} & x^2r_{2x} & xyr_{2x} & x^2r_{2y} & xyr_{2y} \\ yr_{2x} & yr_{2y} & xyr_{2x} & y^2r_{2x} & xyr_{2y} & y^2r_{2y} \end{bmatrix}$$

$$284 \quad \mathbf{b} = -[r_{1t} \ r_{2t} \ xr_{1t} \ xr_{2t} \ yr_{1t} \ yr_{2t}]. \quad (16)$$

285 Note that, according to (12), it is $r_{1x} = \cos^2(\theta)$, $r_{2y} =$
 286 $\sin^2(\theta)$ and $r_{2x} = r_{1y} = \sin(\theta) \cos(\theta)$.

287 B. Multiscale Choice of Window Size

288 The choice of the window size is a tedious issue connected
 289 with local techniques: the assumed motion model (translational
 290 or affine) may not hold when the window is too big, otherwise,
 291 the adoption of an excessively small window may result in
 292 the well known *aperture problem* [34]. To circumvent this
 293 issue, in [20], [21] Sühling *et al.* proposed a multiscale strategy
 294 for locally choosing the most consistent window size. This is
 295 based on the possibility of computing the image moments, *i.e.*,
 296 the entries of the system matrix \mathbf{M} and the vector \mathbf{b} in (16), at
 297 multiple scales, by using an efficient B-spline *coarse-to-fine*
 298 strategy.

299 In particular, they are obtained from window functions w
 300 that are progressively scaled and subsampled by a factor 2
 301 in each dimension. More precisely, at scale j , the window
 302 $w^j(\mathbf{x} - \mathbf{x}_0) = w((\mathbf{x} - 2^j \mathbf{x}_0)/2^j)$ is employed, where w is
 303 written as the separable product of two B-spline functions.

304 By doing so, at each scale $J_f \leq j \leq J_c$ ($J_f \geq 0$) a solu-
 305 tion \mathbf{u}^j can be computed. Among the scales considered, the

Algorithm 1: Multiscale Monogenic Optical Flow

Input: two subsequent frames: I_1, I_2

parameters: $\lambda_0, J_f, J_c, N_p, k, \sigma$.

Output: displacement between I_1 and I_2 : \mathbf{d}

```

d = 0; % initial displacement
for  $i = 1 : N_p$  do % pyramidal refinement
   $[B_e, B_{o1}, B_{o2}] = \text{SQF}(\lambda_0)$ ; % see (2) and (3)
   $[p_1, \mathbf{q}_1] = \text{MonogenSignal}(I_1, B_e, B_{o1}, B_{o2})$ 
   $[p_2, \mathbf{q}_2] = \text{MonogenSignal}(I_2, B_e, B_{o1}, B_{o2})$ 
   $f = \text{MonogenFreq}(p_1, \mathbf{q}_1)$ ; % see (6)
   $\theta = \text{MonogenOrient}(\mathbf{q}_1, \sigma)$ ; % see (10)
   $\mathbf{J} = \text{JacobianMatrix}(f, \theta)$ ; % see (12)
   $\mathbf{r}_t = \text{TimeDer}(p_1, p_2, \mathbf{q}_1, \mathbf{q}_2)$ ; % see (13)
   $\Delta \mathbf{d} = \text{MultiscaleMonogenicOF}(\mathbf{J}, \mathbf{r}_t, J_c, J_f)$ ;
   $\mathbf{d} = \mathbf{d} + \Delta \mathbf{d}$ ; % add increment
   $I_2 = \text{Interp}(I_2, \mathbf{x} + \Delta \mathbf{d})$ ; % warp second frame
   $\lambda_0 = \lambda_0 / k$ ; % decrease wavelength

```

\mathbf{u}^j producing the smallest residual error $\|\mathbf{M}\mathbf{u}^j - \mathbf{b}\|_{\ell_2}/|w|_{\ell_1}$ 306
 is retained as the final displacement estimate. Whenever neces- 307
 sary, bi-cubic interpolation is employed to obtain a dense 308
 motion field. With this strategy, the scale providing the most 309
 consistent motion estimate is selected. 310

311 C. Iterative Displacement Refinement

312 The hypothesis of small displacements employed in differ-
 313 ential techniques may be inadequate whenever the displace-
 314 ment is substantial or the image intensity profile is non-linear.
 315 A possible way to deal with this limitation is to implement
 316 a form of Gauss-Newton optimization: the current estimate is
 317 used to undo the motion, and then the estimator is reapplied to
 318 the warped images to find the residual displacement [24], [31],
 319 [35]. When applied iteratively, this procedure can improve the
 320 estimation accuracy considerably.

321 We employed the aforementioned refinement scheme in
 322 the algorithm presented. In particular, we found it to be
 323 particularly effective when the degree of detail in the mono-
 324 genic phase image progressively increases between subsequent
 325 iterations. In practice, this is established by suitably tuning the
 326 center frequency f_0 of the SQF bank. By doing so, the coarsest
 327 image is first employed to determine a rough estimate of the
 328 displacement. This estimate is then adjusted on the finer detail
 329 data, obtained from an higher value of center frequency.

330 IV. IMPLEMENTATION DETAILS

331 The pseudo-code of the proposed algorithm is pre-
 332 sented in Algorithm 1. The pyramidal refinement scheme of
 333 Section III-C was implemented by decreasing the filter wave-
 334 length λ_0 by a factor $k = 1.5$ at each iteration. The number
 335 of iterations N_p and the starting wavelength value have been
 336 optimized in each of the experiments described in the next
 337 session.

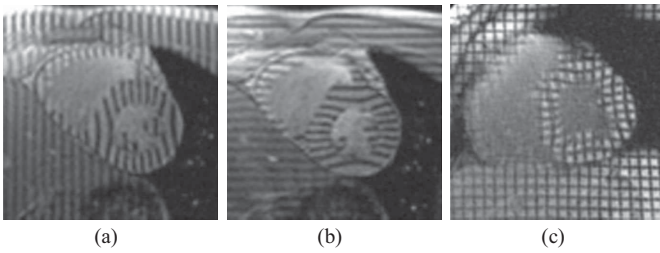


Fig. 2. (a) Vertical, (b) horizontal, and (c) grid tags. Images from [6].

The multiscale window choice was implemented by considering fifth-order B-splines and scales $j = \{2, 3, 4, 5\}$. We note that at scale j the motion is computed on square windows with sides $5 \cdot 2^j - 1$, with a spacing of 2^j pixels between neighboring estimates. A value $\sigma = 2$ was used for the robust computation of the monogenic orientation.

The proposed algorithm has been implemented in MATLAB (R2011b, The Math-Works, Natick, MA). The code is made freely available at <http://www.creatis.insa-lyon.fr/us-tagging/code>.

V. RESULTS

The algorithm was tested on realistic simulated cardiac ultrasound and tagged cardiac MRI (tMRI) image sequences for which the benchmark motion was known. In each case, a comparison will be presented with state-of-the-art algorithms for cardiac motion estimation and with the algorithm of Zang *et al.* [24], which, to the best of our knowledge, is the most closely related work to the study presented in this paper. The Zang algorithm is briefly summarized in Appendix VI.

Concerning performance assessment, the most commonly used measurement in the literature is the angular error [36]. Nevertheless, this metric has several shortcomings. At first, due to the arbitrary scaling constant (1.0) used to avoid the divide-by-zero problem, it penalizes small displacements more than large ones. Second, symmetrical deviations of estimated vectors from the true value result in different error values.

For these reasons, we employ here the less conventional but more appropriate endpoint error (EE) [37], [38]:

$$EE = \|\mathbf{d} - \bar{\mathbf{d}}\|_2 \quad (17)$$

where \mathbf{d} denotes the estimated displacement and $\bar{\mathbf{d}}$ the benchmark displacement.

A. MRI Tagging

1) *Background*: Tagged MRI is currently the gold-standard technique for quantification of myocardial contractility *in vivo* [23], [39]. With this technique, cardiac tissue is marked with magnetically saturated tagging lines or grids (cf. Fig. 2) that deform with the underlying tissue during the cardiac cycle, thus providing details on the myocardial motion. With time elapsing, the grid loses contrast and sharpness [cf. Fig. 3(a)–(c)]. This is the reason why state-of-the-art techniques for the estimation of myocardial motion from tMRI sequences exploit the image phase rather than the less

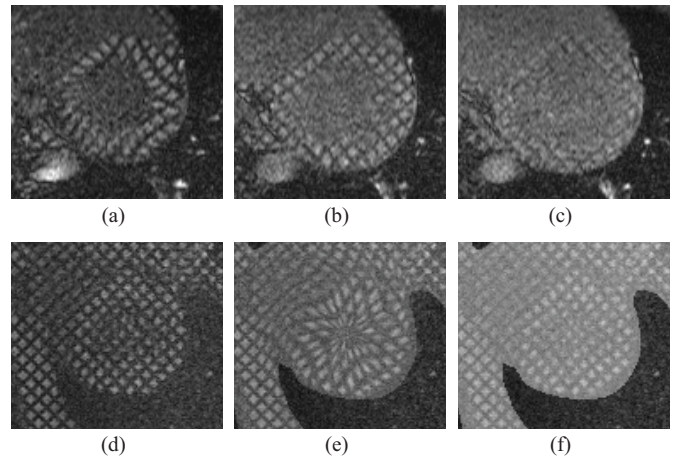


Fig. 3. Tags fading effect on (a)–(c) a real tMRI sequence and (d)–(f) on a simulated one.

trustworthy pixel intensity. The popular algorithms HARP (harmonic phase) [39] and SinMod (sine-wave modeling) [23] belong to this family of methods. In particular, the latter was shown to outperform HARP in [23].

Both the aforementioned algorithms are derived from modeling the tMRI image as the superposition of monochromatic plane waves:

$$I(\mathbf{x}) \approx A(\mathbf{x}) \cos(\omega_0^T \mathbf{x}) \quad (18)$$

where ω_0 is fixed given tags direction and spacing. The displacement is then computed in the Fourier domain from the responses of a set of bandpass directional filters tuned accordingly to ω_0 . More specifically, while HARP [39] employs a phase-based disparity measure similar to the one by Fleet and Jepson [40], SinMod estimates the displacement based on an analytical expression for the cross-power spectrum of two subsequent frames [23].

It is interesting to observe (18) in relation with the work presented here. At first, that model directly satisfies the assumption of 1D local structures, at the base of the monogenic signal analysis. This makes the monogenic signal a promising tool for the study of tMRI sequences. To our knowledge, this is the first study investigating this possibility. Second, (18) can be readily obtained from (1) by including the first-order phase expression used in Section III. This reveals that on tMRI images the assumption of small displacements is no longer required. The upper-limit for the displacement is now given by one-half of the tag spacing, beyond which the motion estimation problem becomes undetermined.

2) *Motion Estimation Results*: The proposed algorithm is compared with SinMod, available in the InTag plugin for OsiriX.¹ The evaluation was made on synthetic tMRI sequences, generated with the ASSESS software [41]. The synthetic motion is established on the basis of a 2D analytical model taking typical contraction, relaxation, torsion and thickening of the cardiac muscle into account [42]. The characteristic tag-fading effect, not considered in ASSESS, was also taken into account in this study, as shown in

¹Available at: <http://www.creatis.insa-lyon.fr/inTag/>.

TABLE I

ENDPOINT ERROR ($\mu \pm \sigma$) IN PIXELS ON NINE SIMULATED SEQUENCES

Sequence	Algorithm		
	Proposed	SinMod	Zang
D30	0.152 \pm 0.121	0.215 \pm 0.145	0.163 \pm 0.137
D30F20	0.082 \pm 0.072	0.128 \pm 0.112	0.087 \pm 0.079
D30R10T01P0	0.264 \pm 0.149	0.363 \pm 0.199	0.303 \pm 0.202
D30R20T01P0	0.462 \pm 0.239	0.970 \pm 1.129	0.531 \pm 0.328
D30R20T01POF20	0.209 \pm 0.139	0.344 \pm 0.224	0.224 \pm 0.174
D30R20T01P3	0.419 \pm 0.228	0.911 \pm 1.099	0.461 \pm 0.301
R20F20	0.244 \pm 0.164	0.416 \pm 0.264	0.247 \pm 0.191
R10	0.161 \pm 0.087	0.220 \pm 0.090	0.164 \pm 0.104
R20	0.104 \pm 0.072	0.174 \pm 0.122	0.124 \pm 0.079

418 Fig. 3(d)–(f). The effect was obtained by adjusting the image’s
 419 histogram limits on each frame so as to match those of a real
 420 sequence taken as a template. The algorithm of Zang *et al.*
 421 [24] was also considered in the comparison.

422 The results obtained on nine simulated sequences are
 423 summarized in Table I. For each algorithm the parameters were
 424 optimized to return the smallest average error on the sequence
 425 D30R20T01POF20. For the proposed algorithm, these values
 426 were $\lambda_0 = 4$ for the initial wavelength and $N_p = 5$ for
 427 the number of refinement steps. For the Zang algorithm,
 428 the values were $\alpha = 0.2$ for the weight between the data
 429 and the smoothness term, $\gamma = 0.1$ for the weight between
 430 the monogenic signal and the monogenic curvature and a
 431 variance ρ^2 of 2 pixels for the Gaussian localizing window
 432 (see Appendix VI for a clearer understanding of the param-
 433 eters’ meaning). A multi-resolution refinement scheme was also
 434 employed [24] with four levels. SinMod required the tags type
 435 (grid), direction (45°) and spacing (six pixels). The name of
 436 each sequence reflects the values of the parameters used for
 437 its generation, namely: contraction/expansion (D), rotation (R),
 438 thickening (T), frame-rate (F) and healthy (P0) or pathological
 439 (P3) state. Greater detail on their meaning can be found
 440 in [42].

441 These results show that the proposed algorithm system-
 442 atically returns the estimate with the smallest mean value
 443 and variance, which is a proof of precision and reliability.
 444 While the improvement with respect to SinMod is evident,
 445 the improvement with respect to the Zang algorithm is less
 446 pronounced. Nevertheless, the differences among all the algo-
 447 rithms were found to be statistically significant ($p < 0.0001$)
 448 for all sequences using the Friedman rank test ($\alpha = 0.05$) in
 449 conjunction with the *post-hoc* test proposed by Daniel [43],
 450 as suggested in [44]. In order to avoid correlations among
 451 samples, we suitably subsample the error images prior to the
 452 statistical analysis.

453 A clearer understanding of the algorithm’s performance is
 454 provided by Fig. 4 where the error dispersion on two of the
 455 simulated sequences is represented for the three algorithms
 456 considered. The sequences were considered in order to present
 457 two different kinds of motions, specifically pure rotation (a)
 458 and pure contraction/expansion (b). In both cases, the proposed
 459 algorithm and Zang’s algorithm outperform SinMod. It is also

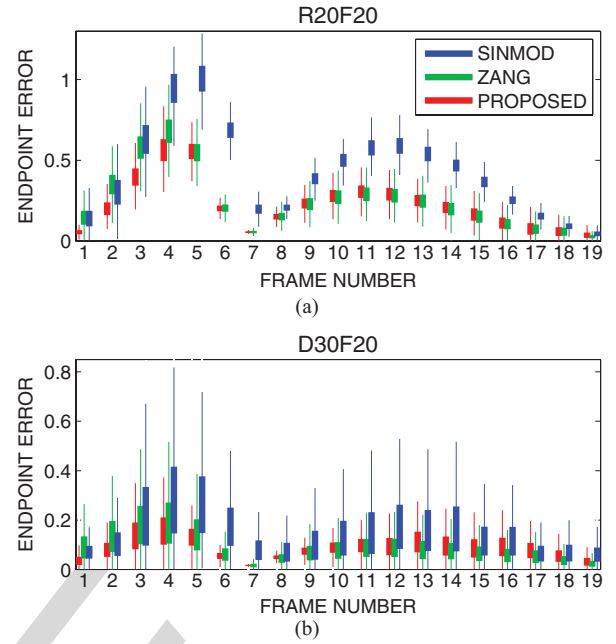


Fig. 4. Boxplot of the errors for (a) R20F20 and (b) D30F20. The center of each box represents the median while the body extends from the 25th to the 75th percentile.

460 clear how the proposed algorithm provides better estimates
 461 than Zang’s in the first part of the sequence, *i.e.* when the
 462 displacements are greater, while, in the final part, the two
 463 estimates are almost equivalent.

464 To better appreciate the difference in performance, it is
 465 useful to analyze the local behavior of each algorithm. This is
 466 represented in Fig. 5, where the error images obtained on the
 467 4-th frame of the two sequences considered above is displayed.
 468 At that instant, the displacement reaches the maximum average
 469 value and the greatest spatial variation in both cases: in the
 470 first case (first row in the Figure) the angular velocity decreases
 471 linearly, passing from the endocardial to the epicardial contour;
 472 in the second (second row in the figure) the radial contraction
 473 is null on the epicardium and maximal on the endocardium.

474 From the comparison between Fig. 5(c)–(g) and
 475 Fig. 5(d)–(h) it is clear how the Zang algorithm suffers
 476 more from these gradients of velocity than the proposed
 477 algorithm. This is a consequence of its global nature. Indeed,
 478 this method imposes a constraint on the gradient of the motion
 479 field that turns out to be inadequate when the entity of the
 480 displacement varies rapidly inside the image. At this point,
 481 it is important to remember that these results correspond to
 482 the optimal parameters’ configuration. In particular, smaller
 483 values of the smoothness weight α , which could tentatively
 484 be employed in order to avoid over-regularization effects,
 485 lead instead to larger errors. For example, a reduction of
 486 α from the optimal 0.2 to 0.05 leads to an increase in the
 487 endpoint error from 0.45 to 0.68 pixels. As shown by the
 488 previous results, SinMod is outperformed by both methods.

489 More generally, Zang’s algorithm appears to involve exces-
 490 sively rigid priors on the displacement model, which makes it
 491 unsuitable to dealing with more complex and inhomogeneous
 492 motion patterns. In contrast, the proposed algorithm does not

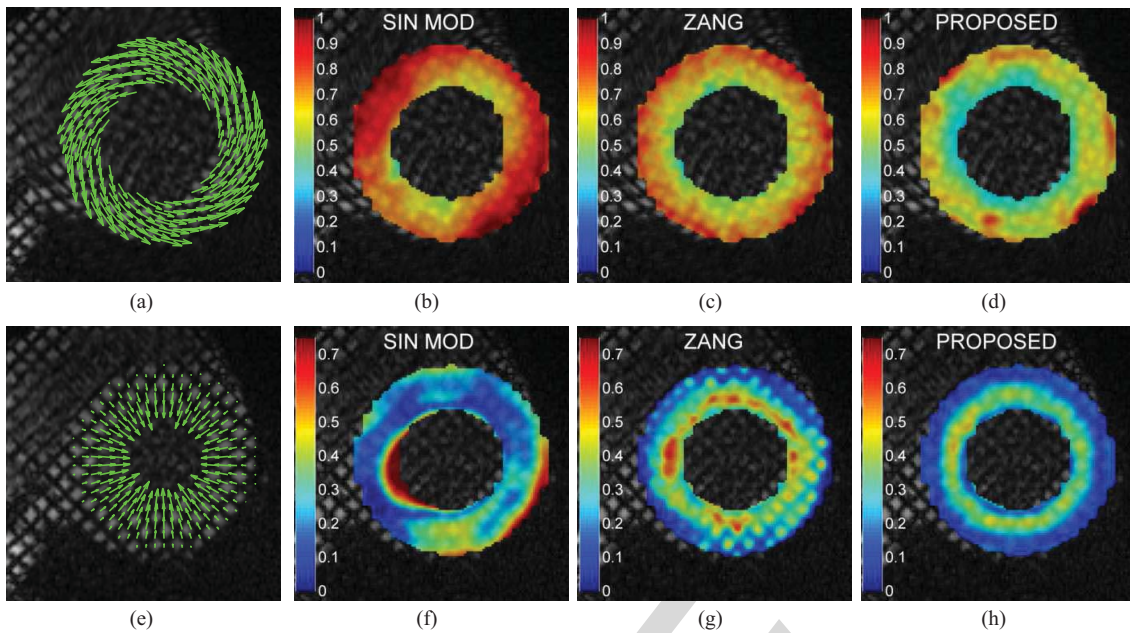


Fig. 5. Error map for the fourth frame. (a)–(d) R20F20. (e)–(h) D30F20. The green arrows in (a) and (e) denote the benchmark field.

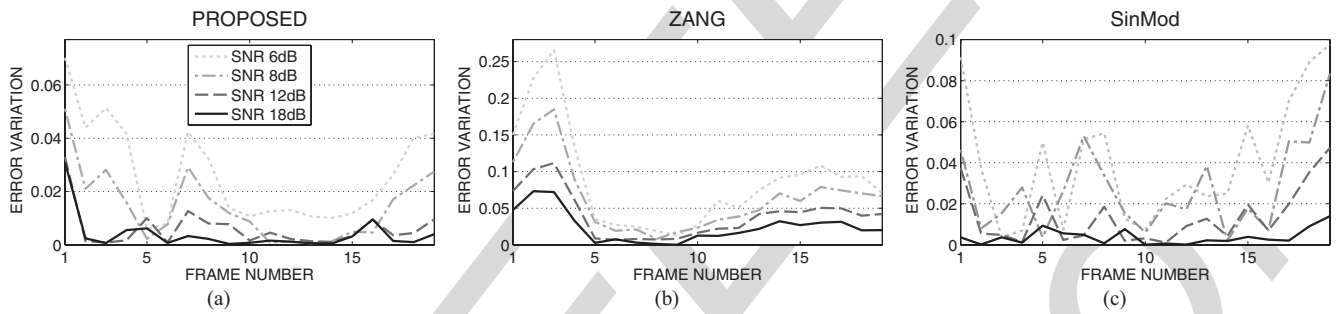


Fig. 6. Sensitivity to noise of (a) proposed algorithm, (b) Zang’s algorithm, and (c) SinMod. Note that different scales have been adopted in the three plots in order to optimize the error range visualization. Indeed, this is substantially different in the three cases. As an example, the average error variation in the 6-dB case is of 0.09 pixels for Zang’s algorithm, 0.04 pixels for SinMod, and 0.02 pixels for the proposed algorithm.

493 imply any hypothesis on the motion field, and therefore it can
494 handle similar situations with superior flexibility.

495 The sensitivity to noise was also evaluated. To this end, we
496 contaminated the frames of sequence R20F20 with additive
497 Rician noise [5]. Fig. 6 reports the endpoint error variation
498 due to noise, *i.e.* the value $|EE_n - EE_{ref}|$, where EE_{ref}
499 is the average endpoint error measured in the noise-free case
500 (cf. Fig. 4), while EE_n is the value in the presence of
501 noise. The results are based on 15 independent noise realiza-
502 tions. While the performance of the Zang algorithm decreases
503 considerably, especially for large motions, the performance
504 of the proposed algorithm remains virtually unchanged. The
505 good robustness against noise stems from two factors: the
506 multiscale window choice of Section III-B and the robust
507 monogenic orientation of Section II-A. The first guarantees
508 that the integration scale is optimized locally so as to minimize
509 the noise effect on the velocity determination, while the second
510 ensures a more robust computation of the monogenic features.
511 We also note that sensitivity to noise is a known drawback
512 of global techniques as compared to local techniques [45].
513 SinMod also shows better noise robustness as compared to the

Zang algorithm. Nevertheless, it should be noted that SinMod
also returned the worst results in terms of accuracy.

514 Here we note that the computation of the monogenic signal
515 involves pre-filtering the data, and this can produce some
516 noise suppression. Nevertheless, this fact does not explain the
517 superiority with respect to Zang’s algorithm given that the
518 latter makes use of the same set of SQF filters that we employ
519 in the proposed method. Instead, the actual difference comes
520 due to the fact that the proposed is a local method, therefore
521 intrinsically less sensitive to noise. Moreover, as previously
522 mentioned, noise robustness is further improved by the use of a
523 multiscale window choice and a robust monogenic orientation
524 computation.
525
526

527 A further fundamental point concerns computational time.
528 For the optimal parameters’ configuration, it was 0.55 s/image
529 for the proposed algorithm (image size, 256×256 pixels²)
530 and 17 s/image for Zang’s algorithm. Both these values refer
531 to MATLAB implementations executed on a desktop PC
532 with a 3.47 GHz Intel Xeon X5690 processor, 12 Gb of
533 RAM and running Windows 7. Although unoptimized for
534 definition, given that MATLAB was used, these results give

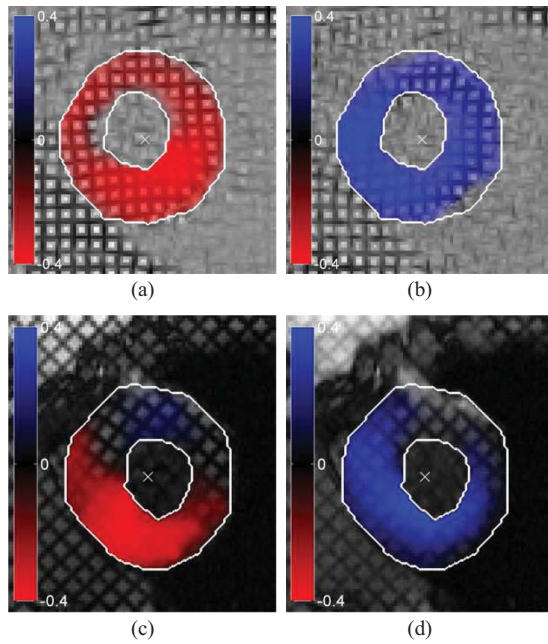


Fig. 7. Color encoding of the radial component of the estimated displacement. Red color encodes inward motion and blue color outward one. No color denotes no motion. The displacement value is expressed in pixel. (a) and (b) present the results on a systolic and diastolic frame on a healthy subject. (c) and (d) present the results on a systolic and diastolic frame on a post-infarction subject. (a) Systole healthy. (b) Diastole healthy. (c) Systole post infarct. (d) Diastole post infarct.

a clear vision on the relation between the complexity of the two algorithms. The increased computational burden of the Zang algorithm is readily explained by its global formulation, demanding the employment of iterative optimization routines, cf. Appendix VI. On the contrary, the proposed algorithm reaches a sub-second speed with its efficient B-spline formalism (even in this unoptimized version). It is worth pointing out that fast computation is primal as far as medical imaging is concerned.

Finally, the feasibility of the algorithm presented in a clinical setting was qualitatively assessed by considering two real acquisitions. The first came from a healthy subject (Siemens MAGNETOM Avanto 1.5T, 6 mm tag-spacing, 0° tag-orientation), the second from a patient who underwent inferior cardiac infarction due to the occlusion of the left anterior descending artery (LAD). This latter acquisition refers to two days after reperfusion (Siemens MAGNETOM Avanto 1.5T, 6 mm tag-spacing, 45° tag-orientation). A qualitative representation of the results is given in Fig. 7. The color map superimposed on the tMRI image encodes the radial component of the estimated displacement computed with respect to the center of the myocardium, represented by a white cross. Red and blue denote inward and outward displacement, respectively.

The first line of figures corresponds to a systolic and diastolic frame on the healthy subject: the estimated displacement reflects the physiological contraction and dilatation of the left ventricle in these two phases of the heart cycle. In contrast, on the post-infarct patient, the color notation reflects the reduced mobility of the heart regions involved in the infarction. More than that, Fig. 7(c) demonstrates a dyskinetic behavior,

represented by an non physiological outward motion during systole [21].

In the experiments illustrated in Fig. 7, the heart mask was drawn manually by a cardiologist and the center point was computed as its center of mass. Several ways for automatizing myocardium tracking on tMRI sequences have been proposed in the literature and could be employed here in lieu of manual contouring. Reviewing them is beyond the scope of this paper.

Clearly, the evaluation proposed above is far from being an exhaustive clinical evaluation of the proposed algorithm. Still, it gives insights into the meaningfulness of the estimates it returns. A deeper evaluation on diagnostic cases is left to further studies.

We conclude this section by noting that, even though the model (18) is adequate for line-tags, otherwise, in the case of grid-tags, a second wave roughly perpendicular to the first should be included in the image model. This would suggest investigating the use of 2D extensions of the monogenic signal. In particular the signal multi-vector [28] shows excellent fit with the grid-tag image model. Similar considerations deserve to be investigated more in depth in future studies. Nonetheless, the results presented here show that, even in the grid-tag case, the monogenic-phase-based algorithm presented still produces relevant estimates.

B. Cardiac Ultrasound

1) *Background:* Quantitative analysis of cardiac ultrasound sequences can provide important mechanical measurements such as muscle strain and twist, wall thickness and ejection fraction [18]. Compared to MRI, medical ultrasound has a higher spatio-temporal resolution, requires no infrastructures, low budgets and involves no discomfort for the patients. For these reasons it is currently the most widespread medical imaging exam [46]. These factors explain the high clinical interest in the development of tools for the determination of cardiac function from cardiac ultrasound images [18].

While tissue Doppler offers a powerful instrument to evaluate cardiac deformation [47], it suffers from the major limitation that only the velocity component in the direction of the ultrasound beam can be determined. This has motivated a growing interest in the development of non-Doppler techniques. They include speckle-tracking [48], frame-to-frame [49] or group-wise elastic registration [33] and optical flow [21]. In particular, the algorithm of Sühling *et al.* [21] achieves an excellent compromise between accuracy and computational complexity. Moreover, its clinical feasibility has been attested in thorough studies [17].

The Sühling algorithm improves the Lucas & Kanade [30] formalism by including the multiscale window choice strategy of Section III-B. As in [30], motion is computed on the basis of the brightness conservation between subsequent frames. Nevertheless, as mentioned in the introduction, this can be a misleading assumption as far as cardiac ultrasound is concerned. This is also proved by the increasing interest in phase-based solutions [11], [14].

The following compares the proposed multiscale monogenic optical-flow algorithm presented in this paper, the Sühling

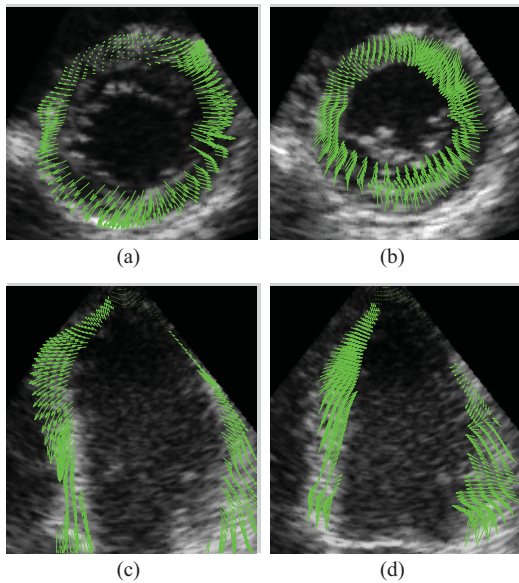


Fig. 8. (a) and (b) Diastolic and systolic frames from a synthetic short axis sequence. The motion estimated with the proposed algorithm is superimposed as green arrows. (c) and (d) Diastolic and systolic frames from a synthetic apical four chambers sequence.

TABLE II
ENDPOINT ERROR ($\mu \pm \sigma$)

Algorithm	Sequence	
	Apical 4 Chambers	Short Axis
Sühling	0.395 ± 0.338	0.396 ± 0.346
Felsberg	0.315 ± 0.257	0.364 ± 0.293
Zang	0.294 ± 0.217	0.324 ± 0.256
Proposed	0.264 ± 0.190	0.313 ± 0.242

algorithm, the Zang algorithm and the Felsberg algorithm, which has been recently applied to medical ultrasound in [50].

2) *Motion Estimation Results:* In order to provide a quantitative evaluation of the algorithms considered, we use synthetic echocardiographic sequences. The simulation framework is described in [51]. The simulated sequences along with the benchmark fields are available for download at <http://www.creatis.insa-lyon.fr/us-tagging/news>. In this study, we assessed two simulated sequences: one Short Axis (SAX) and one Apical 4 Chambers (A4C). These are two of the most frequently adopted orientations in the clinical procedure [52].

A representation of the estimated motion fields with the proposed algorithm is given in Fig. 8. These fields show how the estimates are qualitatively consistent with physiological cardiac motion: indeed the motion vectors point inward during systole and outward during diastole.

Table II reports the average errors obtained on the entire simulated sequences. For all the algorithms, the parameters have been optimized to obtain the smallest average error on the SAX sequence. For the proposed algorithm these are $\lambda_0 = 2$ and $N_p = 5$. For the Zang algorithm they are instead $\gamma = 0.2$, $\alpha = 0.2$, $\rho = 2$ and five pyramidal refinements. The Felsberg algorithm employed a fixed window w given by the tensor

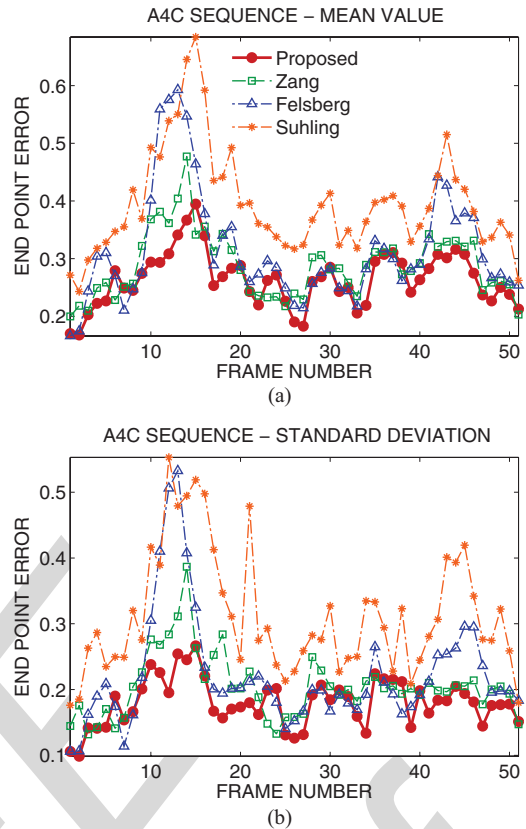


Fig. 9. Endpoint error (in pixels) for the four algorithms on the synthetic A4C sequence (a) mean value and (b) standard deviation.

product of two B-spline functions of order 5 at scale $J = 4$, while the optimal wavelength for the SQF was 3 pixels. The Sühling algorithm employed the multiscale window choice by testing the same scales $j = \{2, 3, 4, 5\}$ as the proposed algorithm. Neither Felsberg's nor Sühling's algorithm applied any refinement scheme like the one in Section III-C (cf. [19], [21]).

From Table II all the three monogenic phase-based algorithms considered perform better than Sühling's algorithm. This confirms that the monogenic phase is a more reliable feature than pixel intensity as far as medical ultrasound is concerned [8], [11], [14]. Also, both the Zang algorithm and the proposed algorithm outperform the Felsberg algorithm due to their more sophisticated formulation. As in the tMRI case, the improvement with respect to the Zang algorithm is less pronounced than with respect to the other two algorithms. Nevertheless, in this case as well, the differences were found to be statistically significant according to a Friedman rank test ($p < 0.0001$, $\alpha = 0.05$).

A more detailed performance analysis is illustrated in Fig. 9, where the four algorithms are compared on the A4C sequence. The four curves represent the mean value (a) and standard deviation (b) of the endpoint error on each frame of the sequence. As in the tMRI case, the improvement of our algorithm with respect to the Zang algorithm is more relevant for large displacements. In particular, they occur during the diastolic expansion, roughly comprised between frame 10 and frame 22 of the simulated sequence. Again, this superiority can

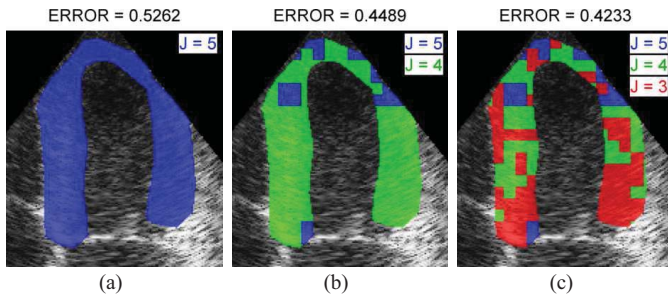


Fig. 10. Color map illustrating the multiscale window choice. Pixels are colored according to the scale determining their velocity. At the initial step (a) only scale $J = 5$ is used, then scale $J = 4$ is tested and (b) displacements are updated where requested by the error criterion. The window choice procedure ends at scale $J = 3$. The title of each figure reports the endpoint error at that step.

673 be explained by the major flexibility involved by the proposed
 674 formalism, which makes it more suitable for following com-
 675 plex motion patterns. The frames between 22 and 44 instead
 676 represent the end of diastole. In this interval, the displacement
 677 is minimal and the Fesberg, Zang and the proposed algorithm
 678 return close results. Finally, the last frames correspond to the
 679 systolic contraction. Here the Zang algorithm and the one
 680 proposed herein still give close estimates, while the error for
 681 the Felsberg algorithm increases. This flaw results from the
 682 absence in the latter of any strategy to account for large
 683 displacements, as the pyramidal refinement adopted in the
 684 Zang algorithm and the proposed algorithm.

685 Finally, Fig. 10 shows the benefits derived from the mul-
 686 tiscale window choice of Section III-B. The color display
 687 represents the scale retained in the velocity computation
 688 while the title reports the corresponding endpoint error. The
 689 progressive error reduction shows how the window selection
 690 procedure allows the computation of more consistent velocity
 691 estimates. The block-like appearance of the color maps results
 692 from the estimate stopping at scale $j = 3$, so that one velocity
 693 is computed every 2^3 pixels. A pixel-wise map is then obtained
 694 by nearest-neighbor interpolation.

695 With respect to Fig. 10, it is also interesting to note that,
 696 while the scale $j = 2$ was also considered, it was never
 697 selected in the velocity computation. This reveals that the
 698 automatic window selection procedure makes the algorithm
 699 almost independent on the chosen range $[J_f, J_c]$.

700 Again, besides being more precise, the proposed algorithm
 701 is somewhat more computationally effective than the Zang
 702 algorithm. As an example, the computation time for one A4C
 703 image (size, 271×333 pixels²) with the optimal parameters
 704 was 0.68 s while it was 18.6 s for the Zang algorithm. This
 705 point is even more important here than with MRI. Indeed,
 706 although off-line processing is considered acceptable in the
 707 latter case, it would not be for ultrasound, where the real-time
 708 aspect is one of the major attractions.

VI. CONCLUSION

710 We have described a novel algorithm for the analysis
 711 of heart motion from medical images. The displacement is
 712 estimated from the monogenic phase and is therefore robust

713 to possible variations of the local image energy. A local affine
 714 model accounts for the typical contraction, torsion and shear
 715 of myocardial fibers. An effective B-spline multiresolution
 716 strategy automatically selects the scale returning the most con-
 717 sistent velocity estimate. The multiresolution strategy together
 718 with a least-squares estimate of the monogenic orientation
 719 make the algorithm robust under image noise.

720 Due to its general formulation, the proposed algorithm is
 721 well suited for measuring myocardial motion from images
 722 from different modalities. In particular, we have presented
 723 an evaluation on cardiac tagged MRI and echocardiographic
 724 sequences. The results have shown that the proposed algorithm
 725 is a valid alternative to state-of-the-art techniques in the two
 726 fields. Moreover, it was shown to be more accurate and
 727 considerably less computation-demanding than another recent
 728 algorithm based on the monogenic signal [24].

729 A potentially valuable application is motion compensation
 730 of myocardial perfusion MRI images [7]. Indeed, the major
 731 challenge in correcting the motion problem is that the local
 732 tissue contrast in the image sequence changes locally with
 733 time, especially in the region of interest, the left ventricular
 734 myocardium. Due to the low sensitivity to alterations in the
 735 brightness profile, we believe the application of the proposed
 736 algorithm to this problem could lead to beneficial results.

APPENDIX

ZANG ALGORITHM FOR OPTICAL FLOW COMPUTATION

737 The Zang algorithm, reported in [24], is based on an
 738 extension of the monogenic signal for intrinsically 2D struc-
 739 tures, called *monogenic curvature tensor*. The motion estimate
 740 is then obtained by plugging this new feature in the popular
 741 non-linear energy function of Bruhn *et al.* [36]:
 742
 743

$$E(\mathbf{w}) = \int_{\Omega} \left(\psi_1 \left(\mathbf{w}^T J_{\rho} (\nabla_3 \varphi + \gamma \nabla_3 \Phi) \mathbf{w} \right) \right) dx dy + \alpha \int_{\Omega} \psi_2 \left(|\nabla \mathbf{w}|^2 \right) dx dy. \quad (19)$$

744 where $\mathbf{w} = [d_1, d_2, 1]$, $\nabla_3 = [\partial_x, \partial_y, \partial_t]$, $J_{\rho} (\nabla_3 f) =$
 745 $K_{\rho} * (\nabla_3 f \nabla_3 f^T)$, $\psi_i(z) = 2\beta_i \sqrt{1 + z/\beta_i}$, α , γ and β are
 746 constant parameters and K_{ρ} is a Gaussian kernel with standard
 747 deviation ρ . The two terms φ and Φ are the monogenic signal
 748 and monogenic curvature phases, respectively.
 749

750 The minimization of (19) is carried out as in [24], [36] with
 751 two nested iterative procedures. An outer fixed point cycle in
 752 ψ_1 , ψ_2 to remove the non-linearity and an inner *successive*
 753 *over-relaxation method* (SOR) to solve the resulting linear
 754 problem. A pyramidal refinement scheme is also employed,
 755 as in [24], [36].
 756

REFERENCES

- 757
 758 [1] M. Felsberg and G. Sommer, "The monogenic signal," *IEEE Trans.*
 759 *Signal Process.*, vol. 49, no. 12, pp. 3136–3144, Dec. 2001.
 760 [2] J. Noble and D. Boukerroui, "Ultrasound image segmentation: A sur-
 761 vey," *IEEE Trans. Med. Imag.*, vol. 25, no. 8, pp. 987–1010, Aug.
 762 2006.
 763 [3] C. Meyer, P. Bland, and J. Pipe, "Retrospective correction of intensity
 764 inhomogeneities in MRI," *IEEE Trans. Med. Imag.*, vol. 14, no. 1, pp.
 765 36–41, Mar. 1995.

- 766 [4] L. Axel and L. Dougherty, "MR imaging of motion with spatial
767 modulation of magnetization," *Radiology*, vol. 171, no. 3, pp. 841–845,
768 Jun. 1989.
- 769 [5] I. Smal, N. Carranza-Herrezuelo, S. Klein, W. Niessen, and E. Meijering,
770 "Quantitative comparison of tracking methods for motion analysis in
771 tagged MRI," in *Proc. IEEE Int. Symp. Biomed. Imag., Nano Macro*,
772 Apr. 2011, pp. 345–348.
- 773 [6] Z. Qian, Q. Liu, D. Metaxas, and L. Axel, "Identifying regional cardiac
774 abnormalities from myocardial strains using nontracking-based strain
775 estimation and spatio-temporal tensor analysis," *IEEE Trans. Med.
776 Imag.*, vol. 30, no. 12, pp. 2017–2029, Dec. 2011.
- 777 [7] N. M. Wilke, M. Jerosch-Herold, A. Zenovich, and A. E. Stillman,
778 "Magnetic resonance first-pass myocardial perfusion imaging: Clinical
779 validation and future applications," *J. Magn. Reson. Imag.*, vol. 10, no. 5,
780 pp. 676–685, 1999.
- 781 [8] M. Mellor and M. Brady, "Phase mutual information as a similarity
782 measure for registration," *Med. Image Anal.*, vol. 9, no. 4, pp. 330–343,
783 2005.
- 784 [9] A. Wong and J. Orchard, "Robust multimodal registration using local
785 phase-coherence representations," *J. Signal Process. Syst.*, vol. 54,
786 nos. 1–3, pp. 89–100, Jan. 2009.
- 787 [10] M. Mulet-Parada and J. Noble, "2D+T acoustic boundary detection in
788 echocardiography," *Med. Image Anal.*, vol. 4, no. 1, pp. 21–30,
789 2000.
- 790 [11] K. Rajnoot, V. Grau, and J. Noble, "Local-phase based 3D boundary
791 detection for real-time 3-D echocardiography," *IEEE Trans. Med. Imag.*,
792 vol. 30, no. 12, pp. 2017–2029, Dec. 2011.
- 793 [12] A. Belkacem, "Phase-based level set segmentation of ultrasound images," *IEEE Trans. Inf. Technol.
794 Biomed.*, vol. 15, no. 1, pp. 138–147, Jan. 2011.
- 795 [13] V. Grau and J. Noble, "Adaptive multiscale ultrasound compounding
796 using phase information," in *Medical Image Computing and Computer-
797 Assisted Intervention* (Lecture Notes in Computer Science), vol. 3749,
798 Berlin, Germany: Springer-Verlag, 2005, pp. 589–596.
- 799 [14] V. Grau, H. Becher, and J. Noble, "Registration of multiview real-time
800 3-D echocardiographic sequences," *IEEE Trans. Med. Imag.*, vol. 26,
801 no. 9, pp. 1154–1165, Sep. 2007.
- 802 [15] N. Chenouard and M. Unser, "3D steerable wavelets and monogenic
803 analysis for bioimaging," in *Proc. IEEE Int. Symp. Biomed. Imag., Nano
804 Macro*, Apr. 2011, pp. 2132–2135.
- 805 [16] C. Wachinger, T. Klein, and N. Navab, "The 2D analytic signal for
806 envelope detection and feature extraction on ultrasound images," *Med.
807 Image Anal.*, vol. 16, no. 6, pp. 1073–1084, 2012.
- 808 [17] M. Sühling, C. Jansen, M. Arigovindan, P. Buser, S. Marsch, M. Unser,
809 and P. Hunziker, "Multiscale motion mapping: A novel computer vision
810 technique for quantitative, objective echocardiographic motion measure-
811 ment independent of doppler: First clinical description and validation,"
812 *Circulation*, vol. 110, no. 19, pp. 3093–3099, Nov. 2004.
- 813 [18] J. D'Hooge, A. Heimdal, F. Jamal, T. Kukulski, B. Bijnens, F. Rade-
814 makers, L. Hatle, P. Suetens, and G. R. Sutherland, "Regional strain and
815 strain rate measurements by cardiac ultrasound: Principles, implementa-
816 tion and limitations," *Eur. J. Echocardiogr.*, vol. 1, no. 3, pp. 154–170,
817 2000.
- 818 [19] M. Felsberg, "Optical flow estimation from monogenic phase," in *Proc.
819 1st Int. Conf. Complex Motion*, 2004, pp. 1–13.
- 820 [20] M. Sühling, M. Arigovindan, P. Hunziker, and M. Unser, "Multires-
821 olution moment filters: Theory and applications," *IEEE Trans. Image
822 Process.*, vol. 13, no. 4, pp. 484–495, Apr. 2004.
- 823 [21] M. Sühling, M. Arigovindan, C. Jansen, P. Hunziker, and M. Unser,
824 "Myocardial motion analysis from B-mode echocardiograms," *IEEE
825 Trans. Image Process.*, vol. 14, no. 4, pp. 525–536, Apr. 2005.
- 826 [22] M. Unser, D. Sage, and D. Van De Ville, "Multiresolution monogenic
827 signal analysis using the Riesz–Laplace wavelet transform," *IEEE Trans.
828 Image Process.*, vol. 18, no. 11, pp. 2402–2418, Nov. 2009.
- 829 [23] T. Arts, F. Prinzen, T. Delhaas, J. Milles, A. Rossi, and P. Clarysse,
830 "Mapping displacement and deformation of the heart with local sine-
831 wave modeling," *IEEE Trans. Med. Imag.*, vol. 29, no. 5, pp. 1114–1123,
832 May 2010.
- 833 [24] D. Zang, L. Wietzke, C. Schmaltz, and G. Sommer, "Dense opti-
834 cal flow estimation from the monogenic curvature tensor," in *Proc.
835 1st Int. Conf. Scale Space Variat. Methods Comput. Vis.*, 2007, pp.
836 239–250.
- 837 [25] M. Felsberg and G. Sommer, "The monogenic scale-space: A unifying
838 approach to phase-based image processing in scale-space," *J. Math.
839 Imag. Vis.*, vol. 21, no. 1, pp. 5–26, 2004.
- 840 [26] G. Granlund and H. Knutsson, *Signal Processing for Computer Vision*.
841 Dordrecht, The Netherlands: Kluwer, 1995.
- 842 [27] D. Boukerroui, J. A. Noble, and M. Brady, "On the choice of band-pass
843 quadrature filters," *J. Math. Imag. Vis.*, vol. 21, no. 1, pp. 53–80, 2004.
- 844 [28] L. Wietzke and G. Sommer, "The signal multi-vector," *J. Math. Imag.
845 Vis.*, vol. 37, no. 2, pp. 132–150, 2010.
- 846 [29] J. Bigun, G. Granlund, and J. Wiklund, "Multidimensional orientation
847 estimation with applications to texture analysis and optical flow," *IEEE
848 Trans. Pattern Anal. Mach. Intell.*, vol. 13, no. 8, pp. 775–790, Aug.
849 1991.
- 850 [30] B. D. Lucas and T. Kanade, "An iterative image registration technique
851 with an application to stereo vision," in *Proc. 7th Int. Joint Conf. Artif.
852 Intell.*, 1981, pp. 674–679.
- 853 [31] J. R. Bergen, P. Anandan, K. J. Hanna, and R. Hingorani, "Hierarchical
854 model-based motion estimation," in *Proc. 2nd Eur. Conf. Comput. Vis.*,
855 1992, pp. 237–252.
- 856 [32] G. Farneback, "Very high accuracy velocity estimation using orienta-
857 tion tensors, parametric motion, and simultaneous segmentation of the
858 motion field," in *Proc. 8th IEEE Int. Conf. Comput. Vis.*, vol. 1, Mar.
859 2001, pp. 171–177.
- 860 [33] M. Ledesma-Carbayo, J. Kybic, M. Desco, A. Santos, M. Sühling,
861 P. Hunziker, and M. Unser, "Spatio-temporal nonrigid registration for
862 ultrasound cardiac motion estimation," *IEEE Trans. Med. Imag.*, vol. 24,
863 no. 9, pp. 1113–1126, Sep. 2005.
- 864 [34] B. K. P. Horn and B. G. Schunck, "Determining optical flow," *Artif.
865 Intell.*, vol. 17, nos. 1–3, pp. 185–203, Aug. 1981.
- 866 [35] C. J. Westelius, "Focus of attention and gaze control for robot vision,"
867 Ph.D. dissertation, Dept. Electr. Eng., Linköping Univ., Linköping,
868 Sweden, 1995.
- 869 [36] A. Bruhn, J. Weickert, and C. Schnörr, "Lucas/Kanade meets Horn-
870 Schunck: Combining local and global optic flow methods," *Int. J.
871 Comput. Vis.*, vol. 61, pp. 211–231, Feb. 2005.
- 872 [37] M. Otte and H. Nagel, "Optical flow estimation: Advances and com-
873 parisons," in *Computer Vision* (Lecture Notes in Computer Science),
874 vol. 800, J.-O. Eklundh, Ed. Berlin, Germany: Springer-Verlag, 1994,
875 pp. 49–60.
- 876 [38] S. Baker, D. Scharstein, J. P. Lewis, S. Roth, M. J. Black, and R. Szeliski,
877 "A database and evaluation methodology for optical flow," *Int. J.
878 Comput. Vis.*, vol. 92, pp. 1–31, Mar. 2011.
- 879 [39] N. Osman, E. McVeigh, and J. Prince, "Imaging heart motion using
880 harmonic phase MRI," *IEEE Trans. Med. Imag.*, vol. 19, no. 3, pp.
881 186–202, Mar. 2000.
- 882 [40] D. J. Fleet and A. D. Jepson, "Computation of component image velocity
883 from local phase information," *Int. J. Comput. Vis.*, vol. 5, no. 1, pp.
884 77–104, Sep. 1990.
- 885 [41] P. Clarysse, J. Tafazzoli, P. Delachartre, and P. Croisille, "Simulation
886 based evaluation of cardiac motion estimation methods in tagged-MR
887 image sequences," *J. Cardiovasc. Magn. Reson.*, vol. 13, p. 360, Feb.
888 2011.
- 889 [42] P. Clarysse, C. Basset, L. Khouas, P. Croisille, D. Friboulet, C. Odet,
890 and I. Magnin, "2D spatial and temporal displacement field fitting from
891 cardiac MR tagging," *Med. Image Anal.*, vol. 3, pp. 253–268, Aug.
892 2000.
- 893 [43] W. Daniel, *Applied Nonparametric Statistics*. Belmont, CA: Duxbury
894 Thomson Learning, 2000.
- 895 [44] V. Chalana and Y. Kim, "A methodology for evaluation of boundary
896 detection algorithms on medical images," *IEEE Trans. Med. Imag.*,
897 vol. 16, no. 5, pp. 642–652, Oct. 1997.
- 898 [45] B. Galvin, B. Mccane, K. Novins, D. Mason, and S. Mills, "Recovering
899 motion fields: An evaluation of eight optical flow algorithms," in *Proc.
900 British Mach. Vis. Conf.*, 1998, pp. 195–204.
- 901 [46] T. L. Szabo, *Diagnostic Ultrasound Imaging: Inside Out*. Burlington,
902 MA: Elsevier, 2004.
- 903 [47] G. R. Sutherland, G. D. Salvo, P. Claus, J. D'Hooge, and B. Bijnens,
904 "Strain and strain rate imaging: A new clinical approach to quantifying
905 regional myocardial function," *J. Amer. Soc. Echocardiogr.*, vol. 17,
906 no. 7, pp. 788–802, 2004.
- 907 [48] T. Marwick, M. Yu, and J. Sun, *Myocardial Imaging: Tissue Doppler
908 and Speckle Tracking*. Oxford, U.K.: Blackwell, 2007.
- 909 [49] J. Kybic and M. Unser, "Fast parametric elastic image registration,"
910 *IEEE Trans. Image Process.*, vol. 12, no. 11, pp. 1427–1442, Nov.
911 2003.
- 912 [50] T. Maltaverne, P. Delachartre, and A. Basarab, "Motion estimation using
913 the monogenic signal applied to ultrasound elastography," in *Proc. Annu.
914 Int. Conf. Eng. Med. Biol. Soc.*, Sep. 2010, pp. 33–36.

- 917 [51] M. Alessandrini, H. Liebgott, D. Friboulet, and O. Bernard, "Simulation
918 of realistic echocardiographic sequences for ground truth validation of
919 motion estimation," in *Proc. IEEE Int. Conf. Image Process.*, Orlando,
920 FL, 2012, pp. 2329–2332.
- 921 [52] T. Dietenbeck, M. Alessandrini, D. Barbosa, J. D'Hooge, D. Fri-
922 boulet, and O. Bernard, "Detection of the whole myocardium in 2D-
923 echocardiography for multiple orientations using a geometrically con-
924 strained level-set," *Med. Image Anal.*, vol. 16, no. 2, pp. 386–401,
925 2012.



Martino Alessandrini received the M.Sc. degree in electronic engineering from the University of Bologna, Bologna, Italy, and the Ph.D. degree from the Advanced Research Center on Electronic Systems for Information and Communication Technologies, Ercole De Castro, Bologna, in 2007 and 2011, respectively.

He is currently a Post-Doctoral Researcher with the Centre de Recherché en Imagerie Médicale (CREATIS), Lyon, France. His current research interests include processing of medical ultrasound

images, with a focus on image restoration, registration, segmentation, despeckling, tissue characterization, and motion tracking techniques.

Dr. Alessandrini was a recipient of the Post-Doctoral Research Grant from CREATIS.



Adrian Basarab received the M.S. and Ph.D. degrees in signal and image processing from the National Institute for Applied Sciences of Lyon, Lyon, France, in 2005 and 2008, respectively.

He has been an Associate Professor with the Université Toulouse III—Paul Sabatier, Toulouse, France, and a member of the Institut de Recherche en Informatique de Toulouse Laboratory (UMR CNRS 5505), Toulouse, since 2009. His current research interests include medical imaging with a focus on motion estimation, inverse problems, and

ultrasound image formation.



Hervé Liebgott received the Master's degree in electrical engineering and the Master's degree in acoustics from the Lyon National Institute of Applied Sciences, Lyon, France in 2002, and the Ph.D. degree with research on transverse oscillations techniques adapted to elastography in 2005. His Ph.D. research involved a six-month visit with the Technical University of Denmark, Kongens Lyngby, Denmark. He received the French Habilitation to Lead Research (HDR) degree from University Lyon 1, Lyon, in 2011.

He is currently an Associate Professor with the Department of Electrical Engineering, University Institute of Technology Lyon 1, Lyon, France, where he is involved in research with a focus on image formation techniques and motion estimation. He is currently the Vice Leader of the Ultrasound Imaging Team, Centre de Recherché en Imagerie Médicale, Lyon, France. He is currently involved in three main research projects: 1) needle biopsy guidance in 3-D ultrasound using matrix arrays; 2) transverse oscillation techniques adapted to echocardiography (the U.S.-Tagging project for which he received a Young Researcher Grant from the French National Research Agency); and 3) application of compressed sensing to medical ultrasound. He conducts research on the processing of medical ultrasound images, with a focus on image restoration, registration, segmentation, despeckling, tissue characterization, and motion tracking techniques. His current research interests include image and signal processing applied to medical ultrasound imaging.



Olivier Bernard received the B.S. and Ph.D. degrees in electrical engineering from the National Institute for Applied Sciences of Lyon (INSA-Lyon), Villeurbanne, France, in 2003 and 2006, respectively.

He was a Post-Doctoral Research Fellow with the Biomedical Imaging Group, École Polytechnique Fédérale de Lausanne, Lausanne, Switzerland, in 2007. He became an Associate Professor with INSA-Lyon and a member of the CREATIS Laboratory (CNRS 5220, INSERM U1044, INSA-Lyon, University of Lyon), Lyon, France, in 2007. His current research interests include biomedical signal and image processing, particularly image segmentation, motion estimation, statistical modeling, and sampling theories.

Dr. Bernard was a recipient of the Special Mention (Second Prize) for the best Ph.D. thesis in France from the IEEE Engineering in Medicine and Biology Society in 2008.

AUTHOR QUERY

AQ:1 = Please confirm the volume no for ref. [13].

I confirm the exactness of the volume number. cf.
http://link.springer.com/chapter/10.1007%2F11566465_73?LI=true

IEEE
Proof

Myocardial Motion Estimation from Medical Images Using the Monogenic Signal

Martino Alessandrini, Adrian Basarab, Hervé Liebgott, and Olivier Bernard

Abstract—We present a method for the analysis of heart motion from medical images. The algorithm exploits monogenic signal theory, recently introduced as an N-dimensional generalization of the analytic signal. The displacement is computed locally by assuming the conservation of the monogenic phase over time. A local affine displacement model is considered to account for typical heart motions as contraction/expansion and shear. A coarse-to-fine B-spline scheme allows a robust and effective computation of the model's parameters, and a pyramidal refinement scheme helps to handle large motions. Robustness against noise is increased by replacing the standard point-wise computation of the monogenic orientation with a robust least-squares orientation estimate. Given its general formulation, the algorithm is well suited for images from different modalities, in particular for those cases where time variant changes of local intensity invalidate the standard brightness constancy assumption. This paper evaluates the method's feasibility on two emblematic cases: cardiac tagged magnetic resonance and cardiac ultrasound. In order to quantify the performance of the proposed method, we made use of realistic synthetic sequences from both modalities for which the benchmark motion is known. A comparison is presented with state-of-the-art methods for cardiac motion analysis. On the data considered, these conventional approaches are outperformed by the proposed algorithm. A recent global optical-flow estimation algorithm based on the monogenic curvature tensor is also considered in the comparison. With respect to the latter, the proposed framework provides, along with higher accuracy, superior robustness to noise and a considerably shorter computation time.

Index Terms—Cardiac ultrasound, illumination changes, iterative refinement, monogenic signal, optical flow, optimal window size, tagged-magnetic resonance imaging (tMRI).

I. INTRODUCTION

THE MONOGENIC signal has been recently introduced by Felsberg [1] as an extension of the analytic signal concept to multiple dimensions. Like the latter, the monogenic signal provides the *local amplitude* and *local phase* signal features. Additionally, it also contains information on the *local orientation*. These three local features are pointwise

Manuscript received March 26, 2012; revised October 17, 2012; accepted October 17, 2012. This work was supported in part by the Agence Nationale de la Recherche under the US-Tagging Grant. The associate editor coordinating the review of this manuscript and approving it for publication was Prof. Richard J. Radke.

M. Alessandrini, H. Liebgott, and O. Bernard are with the Université de Lyon, CREATIS, CNRS UMR5220, Inserm U1044, INSA-Lyon, Université Lyon 1, Lyon 69622, France (e-mail: martino.alessandrini@creatis.insa-lyon.fr; liebgott@creatis.univ-lyon1.fr; olivier.bernard@creatis.insa-lyon.fr).

A. Basarab is with the Institut de Recherche en Informatique de Toulouse, Toulouse CNRS UMR5505, France (e-mail: adrian.basarab@irit.fr).

Color versions of one or more of the figures in this paper are available online at <http://ieeexplore.ieee.org>.

Digital Object Identifier 10.1109/TIP.2012.2226903

orthogonal, which means that they represent independent information: the local amplitude represents the local intensity or dynamics, the local phase describes the local symmetry or grey value transition, and the local orientation describes the direction of the highest signal variance. Decoupling the local energy from the image structure, accounted for by phase and orientation, has made it possible to derive effective solutions to a number of image-processing problems, in particular when the more traditional pixel intensity cannot be considered as a reliable feature.

This situation is often encountered in medical imaging. In cardiac ultrasound, the local brightness varies over time due to the changes in the angle between the myocardial fibers and the direction of propagation of the acoustic beam or due to out-of-plane motions [2]. In magnetic resonance imaging (MRI), intensity variations stem from magnetic field inhomogeneities and scanner-related intensity artifacts [3]. In tagged-MRI (tMRI) [4], tags fade exponentially over time depending on the T1 relaxation time [5], [6]. Obviously, the same problems are encountered when contrast agents are used, such as in perfusion MRI [7] or when registration of images from different modalities, such as computed tomography (CT) and positron emission tomography (PET), is needed [8], [9].

These considerations explain the rapidly growing interest in monogenic signal analysis applied to medical imaging problems over the last few years. For example, one could cite successful applications of monogenic analysis in boundary detection [10], [11], segmentation [12], multi-modal registration [8], [9], ultrasound image compounding [13], multi-view image registration [14], wavelet filtering [15] and envelope detection [16].

In this context, the algorithm presented in this paper, addresses a further fundamental problem in the field of medical imaging, *i.e.* the estimation of myocardial motion. Assessment of myocardial elasticity and contractility is indeed essential in clinical practice to evaluate the degree of ischemia and infraction as well as for surgical planning [17], [18].

We compute the displacement estimate locally by assuming the conservation of the monogenic phase in lieu of traditional pixel brightness. The general formulation takes inspiration from the work of Felsberg in [19]; nevertheless, the novelties with respect to this study are manifold and substantial:

- 1) Locally, the size of the image window is selected in order to have the most consistent motion estimate. This operation is fully automatic and computationally effective because of an adaptation of the B-spline multiresolution approach for the image moments computation proposed by Sühling *et al.* in [20], [21]. By doing

so, a common source of error in local techniques, related to an inadequate choice of the window size, is avoided.

- 2) Felsberg's pure translation model is replaced with an affine model. The affine model, a part of translation, can account for rotation, expansion, compression and shear, and provides a realistic description of the motion patterns typical of the cardiac muscle [17]. Furthermore, as the first-order spatial derivatives of the displacement are also computed, it allows the direct computation of the cardiac strain, with no need for numerical differencing [18].
- 3) The robustness to noise is improved by employing a least squares estimate of the monogenic orientation in place of the standard point-wise estimate [22].
- 4) An incremental *coarse-to-fine* pyramidal scheme is used to refine the precision of the final estimate.

The general formulation makes the algorithm well suited for images from different modalities. In particular, this paper evaluates its performance on tagged magnetic resonance imaging (tMRI) [4] and cardiac ultrasound image sequences. In order to quantify performance, we made use of realistic synthetic sequences for both modalities, for which the benchmark motion was known. In each experiment, a comparison is presented with state-of-the-art methods in the related field. They include SinMod [23] for tMRI images and the Sühling [21] and Felsberg [19] algorithms for ultrasound. In both cases, the recent algorithm reported in Zang *et al.* [24] is also considered in the comparison. Indeed, due to the monogenic signal formulation at its base, it can be considered a possible competitor to the algorithm proposed herein.

The paper proceeds as follows. In Section II the monogenic signal theory is briefly summarized and the robust computation of the orientation is introduced. In Section III the proposed optical flow estimation algorithm is described. Section IV discusses some implementation details. In Section V the problem of cardiac motion analysis from tMRI and cardiac ultrasound is briefly summarized and the results are presented. Concluding remarks are left to Section VI.

II. MONOGENIC SIGNAL COMPUTATION

The most practical aspects of the monogenic signal computation will be reviewed here. For further details, we address the interested reader to [1], [25] and to [22] for a more intuitive derivation.

The monogenic signal provides an extension of the standard analytic signal for multidimensional data. Although the theory is valid for a general number N of dimensions ($N > 1$), we consider here the case at hand of 2D grayscale images $I: \Omega \rightarrow \mathbb{R}, \Omega \subset \mathbb{R}^2$.

The image model adopted in phase-based processing is [19], [26]

$$I(\mathbf{x}) = A(\mathbf{x}) \cos(\varphi(\mathbf{x})) \quad (1)$$

where $\mathbf{x} = [x, y]$ is the spatial coordinate vector, $A(\mathbf{x})$ is the *local amplitude* and $\varphi(\mathbf{x})$ is the *local phase*. Additionally, monogenic signal theory assumes a local intrinsic dimensionality one [19], [26], *i.e.*, the local variations of I are

concentrated along a single direction, defined by the *local orientation* $\theta(\mathbf{x})$.

The monogenic signal computes the image features of amplitude, phase and orientation from the responses to three 2D spherical quadrature filters (SQFs) [1]. The SQFs consist of one *even* rotation invariant bandpass $b_e(\mathbf{x}; \lambda_0)$ filter and two *odd* bandpass filters $b_{o1}(\mathbf{x}; \lambda_0)$ and $b_{o2}(\mathbf{x}; \lambda_0)$, where λ_0 is the filter wavelength, defined as the reciprocal of the normalized center frequency f_0 . Note that in the following the dependency of the filter responses on the center frequency will be omitted for the sake of simplicity. The odd filters are computed from the Riesz transform of the even filter [1], [19]. In the frequency domain it is

$$B_{o1}(\boldsymbol{\omega}) = -\frac{j\omega_x}{|\boldsymbol{\omega}|} \cdot B_e(\boldsymbol{\omega}), \quad B_{o2}(\boldsymbol{\omega}) = -\frac{j\omega_y}{|\boldsymbol{\omega}|} \cdot B_e(\boldsymbol{\omega}) \quad (2)$$

where capital letters denote the Fourier transformed quantities and $\boldsymbol{\omega} = [\omega_x, \omega_y]^T$ is the normalized angular frequency. Several SQF families have been employed in the literature: a comparison of the most popular ones is presented in [27]. A similar study is beyond the scope of this paper. Here, as recommended in [25], [28], the difference of Poisson (DoP) kernel is adopted:

$$B_e(\boldsymbol{\omega}) = \exp(-|\boldsymbol{\omega}|s_1) - \exp(-|\boldsymbol{\omega}|s_2) \quad (3)$$

where $|\boldsymbol{\omega}|$ is the normalized angular frequency and s_1 and $s_2 > s_1$ are two scale parameters. It can be shown that the wavelength is related to the two scales by:

$$\lambda_0 = 2\pi \frac{s_1 - s_2}{\log(s_1) - \log(s_2)}. \quad (4)$$

From the three filter responses, monogenic phase $\varphi(\mathbf{x})$, orientation $\theta(\mathbf{x})$ and amplitude $A(\mathbf{x})$ of I are obtained as:

$$\begin{aligned} \theta(\mathbf{x}) &= \arctan\left(\frac{q_2(\mathbf{x})}{q_1(\mathbf{x})}\right) \\ \varphi(\mathbf{x}) &= \arctan\left(\frac{|\mathbf{q}(\mathbf{x})|}{p(\mathbf{x})}\right) \\ A(\mathbf{x}) &= \sqrt{p^2(\mathbf{x}) + |\mathbf{q}(\mathbf{x})|^2} \end{aligned} \quad (5)$$

where $p(\mathbf{x}) = (I * b_e)(\mathbf{x})$, $q_1(\mathbf{x}) = (I * b_{o1})(\mathbf{x})$, $q_2(\mathbf{x}) = (I * b_{o2})(\mathbf{x})$, $\mathbf{q}(\mathbf{x}) = [q_1(\mathbf{x}), q_2(\mathbf{x})]^T$ and “*” denotes 2D convolution.

From the filter responses, the *local frequency* feature, defined as the derivative of the phase along \mathbf{n} , can also be computed as [19]:

$$f \triangleq (\nabla\varphi)^T \cdot \mathbf{n} = \frac{p\nabla^T \mathbf{q} - \mathbf{q}^T \nabla p}{p^2 + |\mathbf{q}|^2} \quad (6)$$

where $\nabla = [\partial_x, \partial_y]^T$. Dependency on \mathbf{x} is implied.

Monogenic phase and orientation can be conveniently combined in the *phase vector* $\mathbf{r}(\mathbf{x}) = [r_1(\mathbf{x}), r_2(\mathbf{x})] = \varphi(\mathbf{x}) \cdot \mathbf{n}(\mathbf{x})$, with $\mathbf{n}(\mathbf{x}) = [\cos(\theta(\mathbf{x})), \sin(\theta(\mathbf{x}))]^T$ [1], [19]. The dependency on \mathbf{x} of all the aforementioned features will be omitted in the sequel unless necessary.

A. Robust Orientation Computation

In order to improve the robustness against image noise, in this study we replace the classical point-wise estimate of θ (5), with a robust least-squares estimate, inspired by the structure tensor formalism [29]. The scheme presented was proposed by Unser *et al.* in [22].

The least-squares orientation estimate is obtained by maximizing the directional Hilbert transform $\mathcal{H}_\theta I(\mathbf{x})$ averaged over a local neighborhood v_σ

$$\bar{\theta}(\mathbf{x}) = \arg \max_{\theta' \in [-\pi, \pi]} \int_{\mathbb{R}^2} v_\sigma(\mathbf{x}' - \mathbf{x}) \cdot |\mathcal{H}_{\theta'} I(\mathbf{x}')|^2 d\mathbf{x}' \quad (7)$$

where v_σ corresponds here to a Gaussian kernel with variance σ^2 and the directional Hilbert transform is defined in the frequency domain as

$$\mathcal{H}_\theta(\boldsymbol{\omega}) = \frac{\omega_x \cos(\theta) + \omega_y \sin(\theta)}{|\boldsymbol{\omega}|}. \quad (8)$$

It is shown in [22] that (7) corresponds to the classical solution (5) if $v_\sigma(\mathbf{x}) = \delta(\mathbf{x})$. The maximization problem (7) is solved by the eigenvector associated with the largest eigenvalue of the 2×2 matrix $\mathbf{T}(\mathbf{x})$, with entries

$$[\mathbf{T}(\mathbf{x})]_{nm} = \int_{\mathbb{R}^2} v_\sigma(\mathbf{x}' - \mathbf{x}) q_n(\mathbf{x}') q_m(\mathbf{x}') d\mathbf{x}' \quad (9)$$

with $n, m = \{1, 2\}$. The matrix \mathbf{T} can be assimilated to a Riesz-transform counterpart of the standard structure tensor. The new estimate is then given by

$$\bar{\theta}(\mathbf{x}) = \frac{1}{2} \arctan \left(\frac{2[\mathbf{T}(\mathbf{x})]_{12}}{[\mathbf{T}(\mathbf{x})]_{22} - [\mathbf{T}(\mathbf{x})]_{11}} \right). \quad (10)$$

Due to the averaging operation in (7), this alternative estimate is expected to be less sensitive to image noise than the traditional estimate. An example of this property is given in Fig. 1. We conclude this section by noting that this different orientation definition also affects the monogenic phase computation. In particular, the $|\mathbf{q}|$ term appearing in the second equation of (5) must now be replaced with $s(\mathbf{x}) = q_1 \cos \bar{\theta} + q_2 \sin \bar{\theta}$.

III. MULTISCALE OPTICAL FLOW COMPUTATION FROM THE MONOGENIC PHASE

As in [19], the displacement field $\mathbf{d}(\mathbf{x}) = [d_1(\mathbf{x}), d_2(\mathbf{x})]^T$ along x and y between two frames is estimated by replacing the traditional brightness constancy assumption with the more robust *monogenic phase constancy assumption*. This is conveniently expressed in terms of the monogenic phase vector as $\mathbf{r}(\mathbf{x}, t+1) = \mathbf{r}(\mathbf{x} - \mathbf{d}(\mathbf{x}), t)$. Assuming small displacements, the first-order Taylor expansion can be used $\mathbf{r}(\mathbf{x} - \mathbf{d}(\mathbf{x}), t) \approx \mathbf{r}(\mathbf{x}, t) - \mathbf{J}(\mathbf{x}, t) \cdot \mathbf{d}(\mathbf{x})$, where \mathbf{J} is the Jacobian matrix of \mathbf{r} . Then, assuming all points translate of the same quantity \mathbf{d}_0 within a local window w centered in $\mathbf{x}_0 = [x_0, y_0]$, the following linear system of equations is obtained:

$$\begin{aligned} \langle \mathbf{J} \rangle_w \mathbf{d}_0 &= - \langle \mathbf{r}_t \rangle_w, \\ \mathbf{J}(\mathbf{x}, t) &= \begin{bmatrix} r_{1x}(\mathbf{x}, t) & r_{1y}(\mathbf{x}, t) \\ r_{2x}(\mathbf{x}, t) & r_{2y}(\mathbf{x}, t) \end{bmatrix} \end{aligned} \quad (11)$$

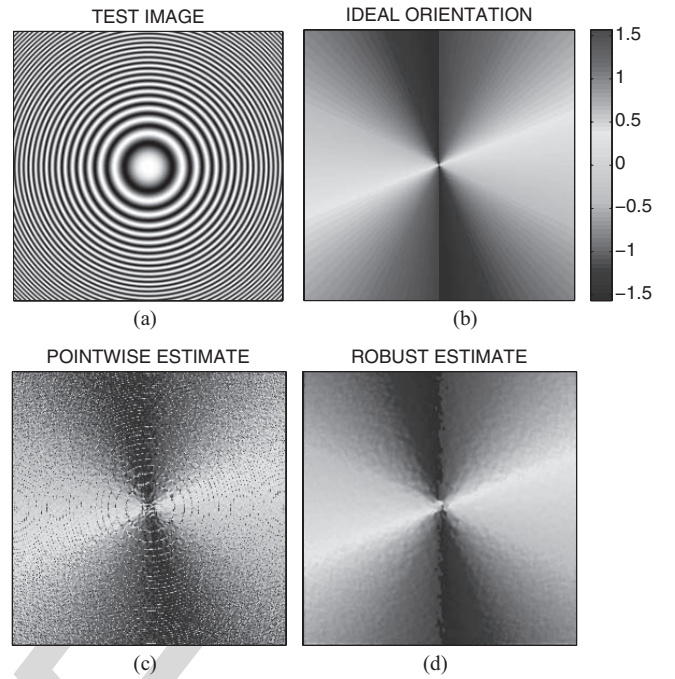


Fig. 1. Monogenic orientation estimate in the presence of noise. (a) Noise-free test image containing a full 360-degree range of orientations. (b) Ideal orientation. (c) and (d) Pointwise and robust ($\sigma = 2$) estimates in the presence of image noise (20 dB). Mean square error of the estimate is $1.2\text{E-}2$ for (c) and $2.7\text{E-}4$ for (d). Phases are wrapped in the $[-\pi/2, \pi/2]$ interval.

where $\mathbf{r}_t(\mathbf{x}, t) = [r_{1t}(\mathbf{x}, t), r_{2t}(\mathbf{x}, t)]$ denotes the time derivative of \mathbf{r} , approximated as $\mathbf{r}(\mathbf{x}, t+1) - \mathbf{r}(\mathbf{x}, t)$, $\langle \mathbf{v} \rangle_w$ denotes the weighted average $\int_{\Omega} w(\mathbf{x} - \mathbf{x}_0) \mathbf{v}(\mathbf{x}) d\mathbf{x}$ and $r_{ik} = \partial_k r_i$. Dependency on (\mathbf{x}, t) will be omitted in the following.

Assuming a 1D structure [19], \mathbf{J} must have rank one. It can be shown that its only eigenvalue corresponds to the monogenic frequency f in (6) while the associated eigenvector is $\mathbf{n} = [\cos(\theta), \sin(\theta)]^T$ [19], [22], this leads to the expression [19], [22]

$$\mathbf{J} = f \mathbf{n} \mathbf{n}^T = f \begin{bmatrix} \cos^2(\theta) & \sin(\theta) \cos(\theta) \\ \sin(\theta) \cos(\theta) & \sin^2(\theta) \end{bmatrix}. \quad (12)$$

The term \mathbf{r}_t is computed from the SQFs responses as [19]:

$$\mathbf{r}_t = \frac{p_t \mathbf{q}_{t+1} - \mathbf{q}_t p_{t+1}}{|p_t \mathbf{q}_{t+1} - \mathbf{q}_t p_{t+1}|} \arctan \left(\frac{|p_t \mathbf{q}_{t+1} - \mathbf{q}_t p_{t+1}|}{p_t p_{t+1} + \mathbf{q}_t^T \mathbf{q}_{t+1}} \right) \quad (13)$$

where subscripts “ t ” and “ $t+1$ ” denote the time instant.

We conclude by noting that (11) represents the monogenic phase counterpart of the popular Lucas & Kanade algorithm [30], where the matrix \mathbf{J} replaces the image structure tensor.

A. Affine Model

Clearly, the simple translation model employed by Felsberg is too restrictive in a general context. Also, its validity is heavily dependent on the choice of the size of w . The solution we propose is to replace the constant motion assumption with a more general model, such as the affine model [31], [32]. A part of translations, this accounts for rotation, expansion, compression and shear. In the context of this paper, the affine

model is of major interest because it provides a realistic description of the motion patterns of the cardiac muscle [17]. A further relevant point is that, as the first-order spatial derivatives of the displacement are also computed, the Lagrangian strain tensor can be directly obtained from the latter, with no need for further numerical differencing. The local analysis of cardiac contractility is indeed fundamental in the diagnosis of pathological situations such as ischemia [18], [33].

Considering for simplicity a window w centered at $(x_0, y_0) = (0, 0)$, the affine model is written:

$$\mathbf{d}(\mathbf{x}) = \mathbf{A}(\mathbf{x})\mathbf{u}, \quad \mathbf{A} = \begin{bmatrix} 1 & 0 & x & y & 0 & 0 \\ 0 & 1 & 0 & 0 & x & y \end{bmatrix} \quad (14)$$

where $\mathbf{u} = [d_{10}, d_{20}, d_{1x}, d_{1y}, d_{2x}, d_{2y}]^T$ is the new unknown vector: d_{10} and d_{20} correspond to the translation of the window center and $d_{ik} = \partial_k d_i$.

Plugging (14) into (11) leads to an underdetermined system of equations. The solution is obtained by pre-multiplying both terms by \mathbf{A}^T , hence

$$\langle \mathbf{M} \rangle_w \mathbf{u} = \langle \mathbf{b} \rangle_w, \quad \mathbf{M} = \mathbf{A}^T \mathbf{J} \mathbf{A}, \quad \mathbf{b} = -\mathbf{A}^T \mathbf{r}_t. \quad (15)$$

Equation (15) represents the proposed monogenic phase version of the Lucas & Kanade algorithm with affine parametrization of the displacement [21].

It can be shown that the entries of \mathbf{M} and \mathbf{b} are the local moments of orders zero to two of the spatial and temporal derivatives of r_1 and r_2 :

$$\mathbf{M} = \begin{bmatrix} r_{1x} & r_{1y} & xr_{1x} & yr_{1x} & xr_{1y} & yr_{1y} \\ r_{2x} & r_{2y} & xr_{2x} & yr_{2x} & xr_{2y} & yr_{2y} \\ xr_{1x} & xr_{1y} & x^2r_{1x} & xyr_{1x} & x^2r_{1y} & xyr_{1y} \\ yr_{1x} & yr_{1y} & xyr_{1x} & y^2r_{1x} & xyr_{1y} & y^2r_{1y} \\ xr_{2x} & xr_{2y} & x^2r_{2x} & xyr_{2x} & x^2r_{2y} & xyr_{2y} \\ yr_{2x} & yr_{2y} & xyr_{2x} & y^2r_{2x} & xyr_{2y} & y^2r_{2y} \end{bmatrix} \quad (16)$$

$$\mathbf{b} = -[r_{1t} \ r_{2t} \ xr_{1t} \ xr_{2t} \ yr_{1t} \ yr_{2t}].$$

Note that, according to (12), it is $r_{1x} = \cos^2(\theta)$, $r_{2y} = \sin^2(\theta)$ and $r_{2x} = r_{1y} = \sin(\theta) \cos(\theta)$.

B. Multiscale Choice of Window Size

The choice of the window size is a tedious issue connected with local techniques: the assumed motion model (translational or affine) may not hold when the window is too big, otherwise, the adoption of an excessively small window may result in the well known *aperture problem* [34]. To circumvent this issue, in [20], [21] Sühling *et al.* proposed a multiscale strategy for locally choosing the most consistent window size. This is based on the possibility of computing the image moments, *i.e.*, the entries of the system matrix \mathbf{M} and the vector \mathbf{b} in (16), at multiple scales, by using an efficient B-spline *coarse-to-fine* strategy.

In particular, they are obtained from window functions w that are progressively scaled and subsampled by a factor 2 in each dimension. More precisely, at scale j , the window $w^j(\mathbf{x} - \mathbf{x}_0) = w((\mathbf{x} - 2^j \mathbf{x}_0)/2^j)$ is employed, where w is written as the separable product of two B-spline functions.

By doing so, at each scale $J_f \leq j \leq J_c$ ($J_f \geq 0$) a solution \mathbf{u}^j can be computed. Among the scales considered, the

Algorithm 1: Multiscale Monogenic Optical Flow

Input: two subsequent frames: I_1, I_2

parameters: $\lambda_0, J_f, J_c, N_p, k, \sigma$.

Output: displacement between I_1 and I_2 : \mathbf{d}

```

d = 0; % initial displacement
for  $i = 1 : N_p$  do % pyramidal refinement
     $[B_e, B_{o1}, B_{o2}] = \text{SQF}(\lambda_0)$ ; % see (2) and (3)
     $[p_1, \mathbf{q}_1] = \text{MonogenSignal}(I_1, B_e, B_{o1}, B_{o2})$ 
     $[p_2, \mathbf{q}_2] = \text{MonogenSignal}(I_2, B_e, B_{o1}, B_{o2})$ 
     $f = \text{MonogenFreq}(p_1, \mathbf{q}_1)$ ; % see (6)
     $\theta = \text{MonogenOrient}(\mathbf{q}_1, \sigma)$ ; % see (10)
     $\mathbf{J} = \text{JacobianMatrix}(f, \theta)$ ; % see (12)
     $\mathbf{r}_t = \text{TimeDer}(p_1, p_2, \mathbf{q}_1, \mathbf{q}_2)$ ; % see (13)
     $\Delta \mathbf{d} = \text{MultiscaleMonogenicOF}(\mathbf{J}, \mathbf{r}_t, J_c, J_f)$ ;
     $\mathbf{d} = \mathbf{d} + \Delta \mathbf{d}$ ; % add increment
     $I_2 = \text{Interp}(I_2, \mathbf{x} + \Delta \mathbf{d})$ ; % warp second frame
     $\lambda_0 = \lambda_0 / k$ ; % decrease wavelength

```

\mathbf{u}^j producing the smallest residual error $\|\mathbf{M}\mathbf{u}^j - \mathbf{b}\|_{\ell_2}/|w|_{\ell_1}$ is retained as the final displacement estimate. Whenever necessary, bi-cubic interpolation is employed to obtain a dense motion field. With this strategy, the scale providing the most consistent motion estimate is selected.

C. Iterative Displacement Refinement

The hypothesis of small displacements employed in differential techniques may be inadequate whenever the displacement is substantial or the image intensity profile is non-linear. A possible way to deal with this limitation is to implement a form of Gauss-Newton optimization: the current estimate is used to undo the motion, and then the estimator is reapplied to the warped images to find the residual displacement [24], [31], [35]. When applied iteratively, this procedure can improve the estimation accuracy considerably.

We employed the aforementioned refinement scheme in the algorithm presented. In particular, we found it to be particularly effective when the degree of detail in the monogenic phase image progressively increases between subsequent iterations. In practice, this is established by suitably tuning the center frequency f_0 of the SQF bank. By doing so, the coarsest image is first employed to determine a rough estimate of the displacement. This estimate is then adjusted on the finer detail data, obtained from an higher value of center frequency.

IV. IMPLEMENTATION DETAILS

The pseudo-code of the proposed algorithm is presented in Algorithm 1. The pyramidal refinement scheme of Section III-C was implemented by decreasing the filter wavelength λ_0 by a factor $k = 1.5$ at each iteration. The number of iterations N_p and the starting wavelength value have been optimized in each of the experiments described in the next session.

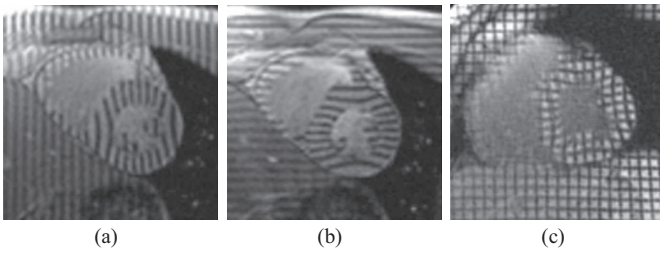


Fig. 2. (a) Vertical, (b) horizontal, and (c) grid tags. Images from [6].

The multiscale window choice was implemented by considering fifth-order B-splines and scales $j = \{2, 3, 4, 5\}$. We note that at scale j the motion is computed on square windows with sides $5 \cdot 2^j - 1$, with a spacing of 2^j pixels between neighboring estimates. A value $\sigma = 2$ was used for the robust computation of the monogenic orientation.

The proposed algorithm has been implemented in MATLAB (R2011b, The Math-Works, Natick, MA). The code is made freely available at <http://www.creatis.insa-lyon.fr/us-tagging/code>.

V. RESULTS

The algorithm was tested on realistic simulated cardiac ultrasound and tagged cardiac MRI (tMRI) image sequences for which the benchmark motion was known. In each case, a comparison will be presented with state-of-the-art algorithms for cardiac motion estimation and with the algorithm of Zang *et al.* [24], which, to the best of our knowledge, is the most closely related work to the study presented in this paper. The Zang algorithm is briefly summarized in Appendix VI.

Concerning performance assessment, the most commonly used measurement in the literature is the angular error [36]. Nevertheless, this metric has several shortcomings. At first, due to the arbitrary scaling constant (1.0) used to avoid the divide-by-zero problem, it penalizes small displacements more than large ones. Second, symmetrical deviations of estimated vectors from the true value result in different error values.

For these reasons, we employ here the less conventional but more appropriate endpoint error (EE) [37], [38]:

$$EE = \|\mathbf{d} - \bar{\mathbf{d}}\|_2 \quad (17)$$

where \mathbf{d} denotes the estimated displacement and $\bar{\mathbf{d}}$ the benchmark displacement.

A. MRI Tagging

1) *Background*: Tagged MRI is currently the gold-standard technique for quantification of myocardial contractility *in vivo* [23], [39]. With this technique, cardiac tissue is marked with magnetically saturated tagging lines or grids (cf. Fig. 2) that deform with the underlying tissue during the cardiac cycle, thus providing details on the myocardial motion. With time elapsing, the grid loses contrast and sharpness [cf. Fig. 3(a)–(c)]. This is the reason why state-of-the-art techniques for the estimation of myocardial motion from tMRI sequences exploit the image phase rather than the less

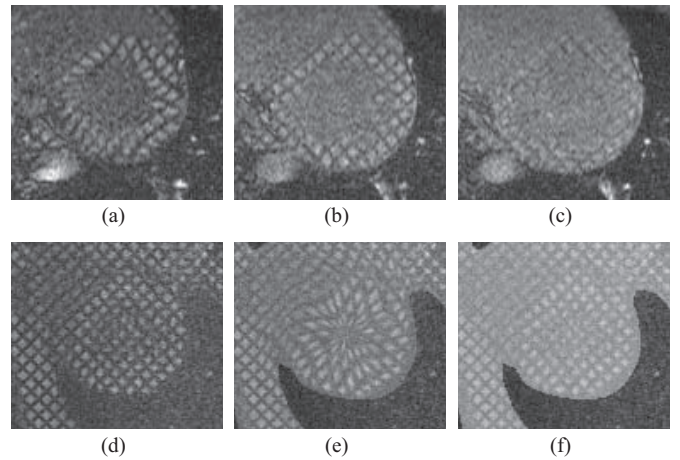


Fig. 3. Tags fading effect on (a)–(c) a real tMRI sequence and (d)–(f) on a simulated one.

trustworthy pixel intensity. The popular algorithms HARP (harmonic phase) [39] and SinMod (sine-wave modeling) [23] belong to this family of methods. In particular, the latter was shown to outperform HARP in [23].

Both the aforementioned algorithms are derived from modeling the tMRI image as the superposition of monochromatic plane waves:

$$I(\mathbf{x}) \approx A(\mathbf{x}) \cos(\omega_0^T \mathbf{x}) \quad (18)$$

where ω_0 is fixed given tags direction and spacing. The displacement is then computed in the Fourier domain from the responses of a set of bandpass directional filters tuned accordingly to ω_0 . More specifically, while HARP [39] employs a phase-based disparity measure similar to the one by Fleet and Jepson [40], SinMod estimates the displacement based on an analytical expression for the cross-power spectrum of two subsequent frames [23].

It is interesting to observe (18) in relation with the work presented here. At first, that model directly satisfies the assumption of 1D local structures, at the base of the monogenic signal analysis. This makes the monogenic signal a promising tool for the study of tMRI sequences. To our knowledge, this is the first study investigating this possibility. Second, (18) can be readily obtained from (1) by including the first-order phase expression used in Section III. This reveals that on tMRI images the assumption of small displacements is no longer required. The upper-limit for the displacement is now given by one-half of the tag spacing, beyond which the motion estimation problem becomes undetermined.

2) *Motion Estimation Results*: The proposed algorithm is compared with SinMod, available in the InTag plugin for OsiriX.¹ The evaluation was made on synthetic tMRI sequences, generated with the ASSESS software [41]. The synthetic motion is established on the basis of a 2D analytical model taking typical contraction, relaxation, torsion and thickening of the cardiac muscle into account [42]. The characteristic tag-fading effect, not considered in ASSESS, was also taken into account in this study, as shown in

¹Available at: <http://www.creatis.insa-lyon.fr/inTag/>.

TABLE I

ENDPOINT ERROR ($\mu \pm \sigma$) IN PIXELS ON NINE SIMULATED SEQUENCES

Sequence	Algorithm		
	Proposed	SinMod	Zang
D30	0.152 \pm 0.121	0.215 \pm 0.145	0.163 \pm 0.137
D30F20	0.082 \pm 0.072	0.128 \pm 0.112	0.087 \pm 0.079
D30R10T01P0	0.264 \pm 0.149	0.363 \pm 0.199	0.303 \pm 0.202
D30R20T01P0	0.462 \pm 0.239	0.970 \pm 1.129	0.531 \pm 0.328
D30R20T01POF20	0.209 \pm 0.139	0.344 \pm 0.224	0.224 \pm 0.174
D30R20T01P3	0.419 \pm 0.228	0.911 \pm 1.099	0.461 \pm 0.301
R20F20	0.244 \pm 0.164	0.416 \pm 0.264	0.247 \pm 0.191
R10	0.161 \pm 0.087	0.220 \pm 0.090	0.164 \pm 0.104
R20	0.104 \pm 0.072	0.174 \pm 0.122	0.124 \pm 0.079

418 Fig. 3(d)–(f). The effect was obtained by adjusting the image’s
 419 histogram limits on each frame so as to match those of a real
 420 sequence taken as a template. The algorithm of Zang *et al.*
 421 [24] was also considered in the comparison.

422 The results obtained on nine simulated sequences are
 423 summarized in Table I. For each algorithm the parameters were
 424 optimized to return the smallest average error on the sequence
 425 D30R20T01POF20. For the proposed algorithm, these values
 426 were $\lambda_0 = 4$ for the initial wavelength and $N_p = 5$ for
 427 the number of refinement steps. For the Zang algorithm,
 428 the values were $\alpha = 0.2$ for the weight between the data
 429 and the smoothness term, $\gamma = 0.1$ for the weight between
 430 the monogenic signal and the monogenic curvature and a
 431 variance ρ^2 of 2 pixels for the Gaussian localizing window
 432 (see Appendix VI for a clearer understanding of the param-
 433 eters’ meaning). A multi-resolution refinement scheme was also
 434 employed [24] with four levels. SinMod required the tags type
 435 (grid), direction (45°) and spacing (six pixels). The name of
 436 each sequence reflects the values of the parameters used for
 437 its generation, namely: contraction/expansion (D), rotation (R),
 438 thickening (T), frame-rate (F) and healthy (P0) or pathological
 439 (P3) state. Greater detail on their meaning can be found
 440 in [42].

441 These results show that the proposed algorithm system-
 442 atically returns the estimate with the smallest mean value
 443 and variance, which is a proof of precision and reliability.
 444 While the improvement with respect to SinMod is evident,
 445 the improvement with respect to the Zang algorithm is less
 446 pronounced. Nevertheless, the differences among all the algo-
 447 rithms were found to be statistically significant ($p < 0.0001$)
 448 for all sequences using the Friedman rank test ($\alpha = 0.05$) in
 449 conjunction with the *post-hoc* test proposed by Daniel [43],
 450 as suggested in [44]. In order to avoid correlations among
 451 samples, we suitably subsample the error images prior to the
 452 statistical analysis.

453 A clearer understanding of the algorithm’s performance is
 454 provided by Fig. 4 where the error dispersion on two of the
 455 simulated sequences is represented for the three algorithms
 456 considered. The sequences were considered in order to present
 457 two different kinds of motions, specifically pure rotation (a)
 458 and pure contraction/expansion (b). In both cases, the proposed
 459 algorithm and Zang’s algorithm outperform SinMod. It is also

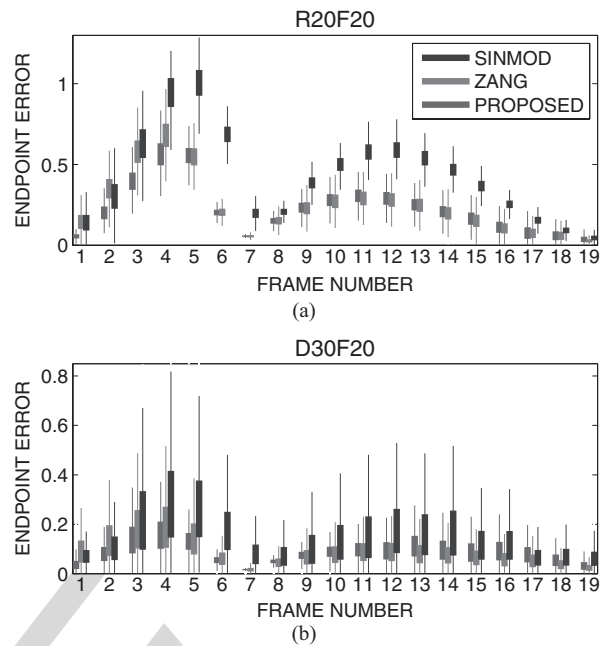


Fig. 4. Boxplot of the errors for (a) R20F20 and (b) D30F20. The center of each box represents the median while the body extends from the 25th to the 75th percentile.

460 clear how the proposed algorithm provides better estimates
 461 than Zang’s in the first part of the sequence, *i.e.* when the
 462 displacements are greater, while, in the final part, the two
 463 estimates are almost equivalent.

464 To better appreciate the difference in performance, it is
 465 useful to analyze the local behavior of each algorithm. This is
 466 represented in Fig. 5, where the error images obtained on the
 467 4-th frame of the two sequences considered above is displayed.
 468 At that instant, the displacement reaches the maximum average
 469 value and the greatest spatial variation in both cases: in the
 470 first case (first row in the Figure) the angular velocity decreases
 471 linearly, passing from the endocardial to the epicardial contour;
 472 in the second (second row in the figure) the radial contraction
 473 is null on the epicardium and maximal on the endocardium.

474 From the comparison between Fig. 5(c)–(g) and
 475 Fig. 5(d)–(h) it is clear how the Zang algorithm suffers
 476 more from these gradients of velocity than the proposed
 477 algorithm. This is a consequence of its global nature. Indeed,
 478 this method imposes a constraint on the gradient of the motion
 479 field that turns out to be inadequate when the entity of the
 480 displacement varies rapidly inside the image. At this point,
 481 it is important to remember that these results correspond to
 482 the optimal parameters’ configuration. In particular, smaller
 483 values of the smoothness weight α , which could tentatively
 484 be employed in order to avoid over-regularization effects,
 485 lead instead to larger errors. For example, a reduction of
 486 α from the optimal 0.2 to 0.05 leads to an increase in the
 487 endpoint error from 0.45 to 0.68 pixels. As shown by the
 488 previous results, SinMod is outperformed by both methods.

489 More generally, Zang’s algorithm appears to involve exces-
 490 sively rigid priors on the displacement model, which makes it
 491 unsuitable to dealing with more complex and inhomogeneous
 492 motion patterns. In contrast, the proposed algorithm does not

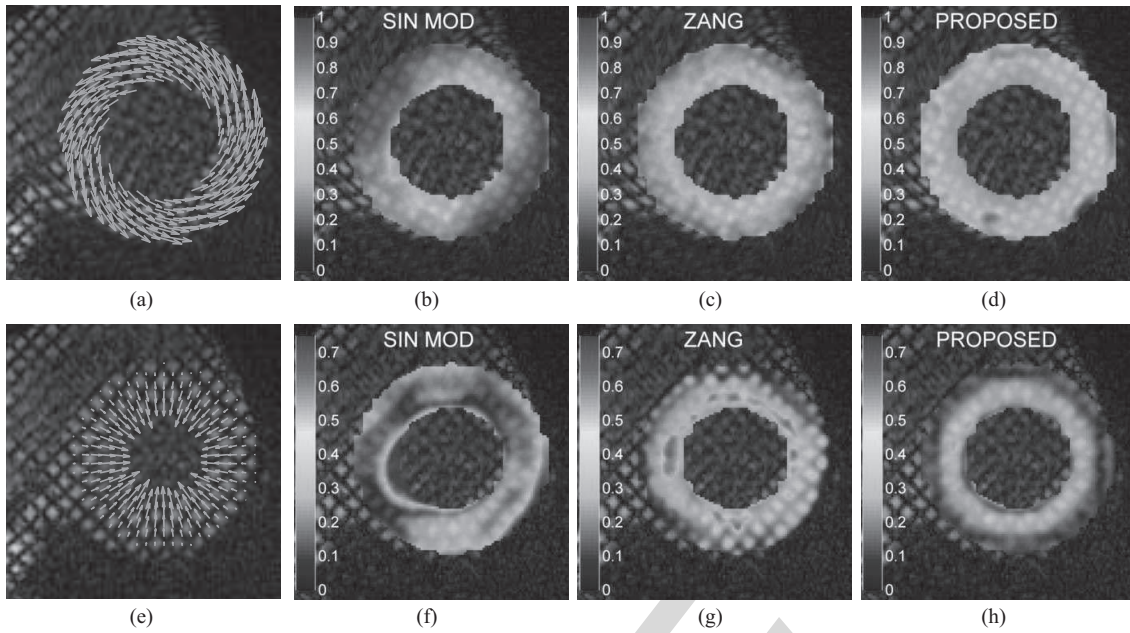


Fig. 5. Error map for the fourth frame. (a)–(d) R20F20. (e)–(h) D30F20. The green arrows in (a) and (e) denote the benchmark field.

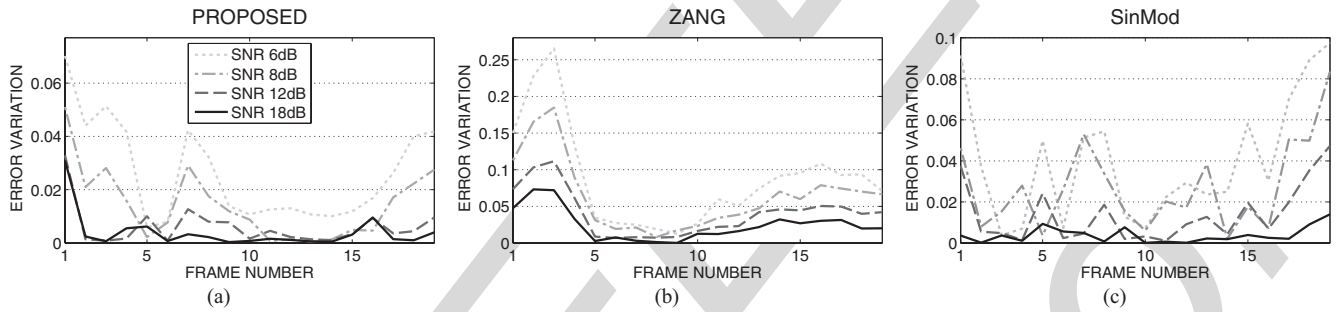


Fig. 6. Sensitivity to noise of (a) proposed algorithm, (b) Zang’s algorithm, and (c) SinMod. Note that different scales have been adopted in the three plots in order to optimize the error range visualization. Indeed, this is substantially different in the three cases. As an example, the average error variation in the 6-dB case is of 0.09 pixels for Zang’s algorithm, 0.04 pixels for SinMod, and 0.02 pixels for the proposed algorithm.

493 imply any hypothesis on the motion field, and therefore it can
494 handle similar situations with superior flexibility.

495 The sensitivity to noise was also evaluated. To this end, we
496 contaminated the frames of sequence R20F20 with additive
497 Rician noise [5]. Fig. 6 reports the endpoint error variation
498 due to noise, *i.e.* the value $|EE_n - EE_{ref}|$, where EE_{ref}
499 is the average endpoint error measured in the noise-free case
500 (cf. Fig. 4), while EE_n is the value in the presence of
501 noise. The results are based on 15 independent noise realiza-
502 tions. While the performance of the Zang algorithm decreases
503 considerably, especially for large motions, the performance
504 of the proposed algorithm remains virtually unchanged. The
505 good robustness against noise stems from two factors: the
506 multiscale window choice of Section III-B and the robust
507 monogenic orientation of Section II-A. The first guarantees
508 that the integration scale is optimized locally so as to minimize
509 the noise effect on the velocity determination, while the second
510 ensures a more robust computation of the monogenic features.
511 We also note that sensitivity to noise is a known drawback
512 of global techniques as compared to local techniques [45].
513 SinMod also shows better noise robustness as compared to the

Zang algorithm. Nevertheless, it should be noted that SinMod
also returned the worst results in terms of accuracy.

514 Here we note that the computation of the monogenic signal
515 involves pre-filtering the data, and this can produce some
516 noise suppression. Nevertheless, this fact does not explain the
517 superiority with respect to Zang’s algorithm given that the
518 latter makes use of the same set of SQF filters that we employ
519 in the proposed method. Instead, the actual difference comes
520 due to the fact that the proposed is a local method, therefore
521 intrinsically less sensitive to noise. Moreover, as previously
522 mentioned, noise robustness is further improved by the use of a
523 multiscale window choice and a robust monogenic orientation
524 computation.
525
526

527 A further fundamental point concerns computational time.
528 For the optimal parameters’ configuration, it was 0.55 s/image
529 for the proposed algorithm (image size, 256×256 pixels²)
530 and 17 s/image for Zang’s algorithm. Both these values refer
531 to MATLAB implementations executed on a desktop PC
532 with a 3.47 GHz Intel Xeon X5690 processor, 12 Gb of
533 RAM and running Windows 7. Although unoptimized for
534 definition, given that MATLAB was used, these results give

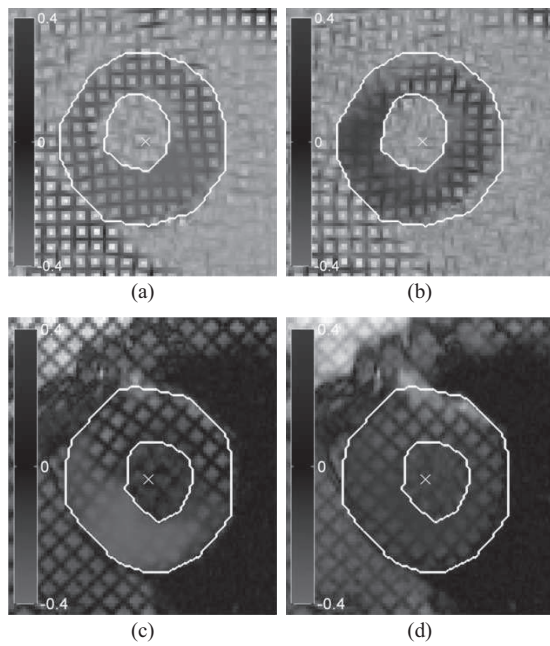


Fig. 7. Color encoding of the radial component of the estimated displacement. Red color encodes inward motion and blue color outward one. No color denotes no motion. The displacement value is expressed in pixel. (a) and (b) present the results on a systolic and diastolic frame on a healthy subject. (c) and (d) present the results on a systolic and diastolic frame on a post-infarction subject. (a) Systole healthy. (b) Diastole healthy. (c) Systole post infarct. (d) Diastole post infarct.

a clear vision on the relation between the complexity of the two algorithms. The increased computational burden of the Zang algorithm is readily explained by its global formulation, demanding the employment of iterative optimization routines, cf. Appendix VI. On the contrary, the proposed algorithm reaches a sub-second speed with its efficient B-spline formalism (even in this unoptimized version). It is worth pointing out that fast computation is primal as far as medical imaging is concerned.

Finally, the feasibility of the algorithm presented in a clinical setting was qualitatively assessed by considering two real acquisitions. The first came from a healthy subject (Siemens MAGNETOM Avanto 1.5T, 6 mm tag-spacing, 0° tag-orientation), the second from a patient who underwent inferior cardiac infarction due to the occlusion of the left anterior descending artery (LAD). This latter acquisition refers to two days after reperfusion (Siemens MAGNETOM Avanto 1.5T, 6 mm tag-spacing, 45° tag-orientation). A qualitative representation of the results is given in Fig. 7. The color map superimposed on the tMRI image encodes the radial component of the estimated displacement computed with respect to the center of the myocardium, represented by a white cross. Red and blue denote inward and outward displacement, respectively.

The first line of figures corresponds to a systolic and diastolic frame on the healthy subject: the estimated displacement reflects the physiological contraction and dilatation of the left ventricle in these two phases of the heart cycle. In contrast, on the post-infarct patient, the color notation reflects the reduced mobility of the heart regions involved in the infarction. More than that, Fig. 7(c) demonstrates a dyskinetic behavior,

represented by a non physiological outward motion during systole [21].

In the experiments illustrated in Fig. 7, the heart mask was drawn manually by a cardiologist and the center point was computed as its center of mass. Several ways for automatizing myocardium tracking on tMRI sequences have been proposed in the literature and could be employed here in lieu of manual contouring. Reviewing them is beyond the scope of this paper.

Clearly, the evaluation proposed above is far from being an exhaustive clinical evaluation of the proposed algorithm. Still, it gives insights into the meaningfulness of the estimates it returns. A deeper evaluation on diagnostic cases is left to further studies.

We conclude this section by noting that, even though the model (18) is adequate for line-tags, otherwise, in the case of grid-tags, a second wave roughly perpendicular to the first should be included in the image model. This would suggest investigating the use of 2D extensions of the monogenic signal. In particular the signal multi-vector [28] shows excellent fit with the grid-tag image model. Similar considerations deserve to be investigated more in depth in future studies. Nonetheless, the results presented here show that, even in the grid-tag case, the monogenic-phase-based algorithm presented still produces relevant estimates.

B. Cardiac Ultrasound

1) *Background*: Quantitative analysis of cardiac ultrasound sequences can provide important mechanical measurements such as muscle strain and twist, wall thickness and ejection fraction [18]. Compared to MRI, medical ultrasound has a higher spatio-temporal resolution, requires no infrastructures, low budgets and involves no discomfort for the patients. For these reasons it is currently the most widespread medical imaging exam [46]. These factors explain the high clinical interest in the development of tools for the determination of cardiac function from cardiac ultrasound images [18].

While tissue Doppler offers a powerful instrument to evaluate cardiac deformation [47], it suffers from the major limitation that only the velocity component in the direction of the ultrasound beam can be determined. This has motivated a growing interest in the development of non-Doppler techniques. They include speckle-tracking [48], frame-to-frame [49] or group-wise elastic registration [33] and optical flow [21]. In particular, the algorithm of Sühling *et al.* [21] achieves an excellent compromise between accuracy and computational complexity. Moreover, its clinical feasibility has been attested in thorough studies [17].

The Sühling algorithm improves the Lucas & Kanade [30] formalism by including the multiscale window choice strategy of Section III-B. As in [30], motion is computed on the basis of the brightness conservation between subsequent frames. Nevertheless, as mentioned in the introduction, this can be a misleading assumption as far as cardiac ultrasound is concerned. This is also proved by the increasing interest in phase-based solutions [11], [14].

The following compares the proposed multiscale monogenic optical-flow algorithm presented in this paper, the Sühling

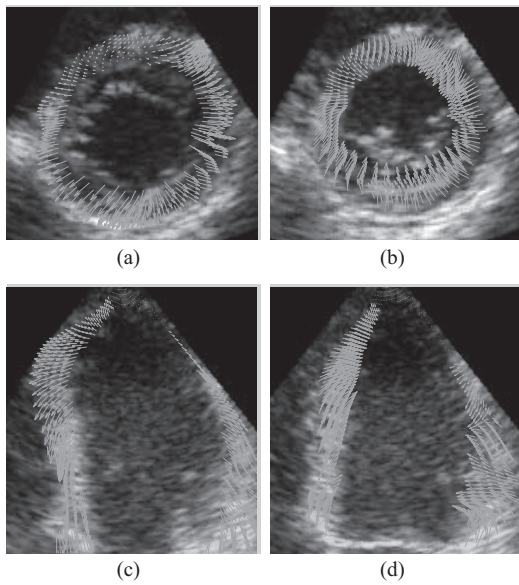


Fig. 8. (a) and (b) Diastolic and systolic frames from a synthetic short axis sequence. The motion estimated with the proposed algorithm is superimposed as green arrows. (c) and (d) Diastolic and systolic frames from a synthetic apical four chambers sequence.

TABLE II
ENDPOINT ERROR ($\mu \pm \sigma$)

Algorithm	Sequence	
	Apical 4 Chambers	Short Axis
Sühling	0.395 ± 0.338	0.396 ± 0.346
Felsberg	0.315 ± 0.257	0.364 ± 0.293
Zang	0.294 ± 0.217	0.324 ± 0.256
Proposed	0.264 ± 0.190	0.313 ± 0.242

algorithm, the Zang algorithm and the Felsberg algorithm, which has been recently applied to medical ultrasound in [50].

2) *Motion Estimation Results:* In order to provide a quantitative evaluation of the algorithms considered, we use synthetic echocardiographic sequences. The simulation framework is described in [51]. The simulated sequences along with the benchmark fields are available for download at <http://www.creatis.insa-lyon.fr/us-tagging/news>. In this study, we assessed two simulated sequences: one Short Axis (SAx) and one Apical 4 Chambers (A4C). These are two of the most frequently adopted orientations in the clinical procedure [52].

A representation of the estimated motion fields with the proposed algorithm is given in Fig. 8. These fields show how the estimates are qualitatively consistent with physiological cardiac motion: indeed the motion vectors point inward during systole and outward during diastole.

Table II reports the average errors obtained on the entire simulated sequences. For all the algorithms, the parameters have been optimized to obtain the smallest average error on the SAx sequence. For the proposed algorithm these are $\lambda_0 = 2$ and $N_p = 5$. For the Zang algorithm they are instead $\gamma = 0.2$, $\alpha = 0.2$, $\rho = 2$ and five pyramidal refinements. The Felsberg algorithm employed a fixed window w given by the tensor

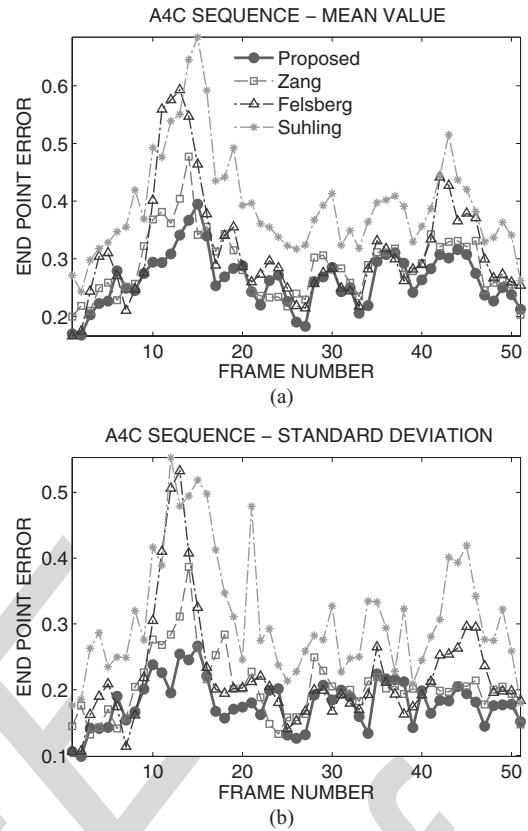


Fig. 9. Endpoint error (in pixels) for the four algorithms on the synthetic A4C sequence (a) mean value and (b) standard deviation.

product of two B-spline functions of order 5 at scale $J = 4$, while the optimal wavelength for the SQF was 3 pixels. The Sühling algorithm employed the multiscale window choice by testing the same scales $j = \{2, 3, 4, 5\}$ as the proposed algorithm. Neither Felsberg's nor Sühling's algorithm applied any refinement scheme like the one in Section III-C (cf. [19], [21]).

From Table II all the three monogenic phase-based algorithms considered perform better than Sühling's algorithm. This confirms that the monogenic phase is a more reliable feature than pixel intensity as far as medical ultrasound is concerned [8], [11], [14]. Also, both the Zang algorithm and the proposed algorithm outperform the Felsberg algorithm due to their more sophisticated formulation. As in the tMRI case, the improvement with respect to the Zang algorithm is less pronounced than with respect to the other two algorithms. Nevertheless, in this case as well, the differences were found to be statistically significant according to a Friedman rank test ($p < 0.0001$, $\alpha = 0.05$).

A more detailed performance analysis is illustrated in Fig. 9, where the four algorithms are compared on the A4C sequence. The four curves represent the mean value (a) and standard deviation (b) of the endpoint error on each frame of the sequence. As in the tMRI case, the improvement of our algorithm with respect to the Zang algorithm is more relevant for large displacements. In particular, they occur during the diastolic expansion, roughly comprised between frame 10 and frame 22 of the simulated sequence. Again, this superiority can

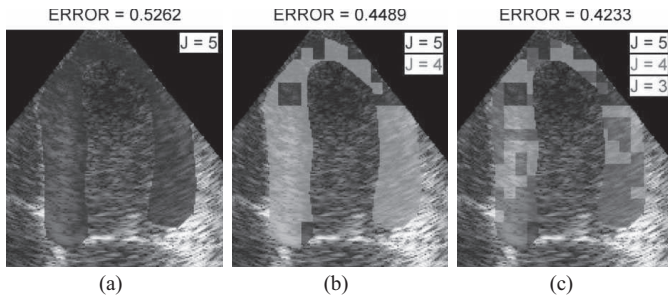


Fig. 10. Color map illustrating the multiscale window choice. Pixels are colored according to the scale determining their velocity. At the initial step (a) only scale $J = 5$ is used, then scale $J = 4$ is tested and (b) displacements are updated where requested by the error criterion. The window choice procedure ends at scale $J = 3$. The title of each figure reports the endpoint error at that step.

673 be explained by the major flexibility involved by the proposed
 674 formalism, which makes it more suitable for following com-
 675 plex motion patterns. The frames between 22 and 44 instead
 676 represent the end of diastole. In this interval, the displacement
 677 is minimal and the Fesberg, Zang and the proposed algorithm
 678 return close results. Finally, the last frames correspond to the
 679 systolic contraction. Here the Zang algorithm and the one
 680 proposed herein still give close estimates, while the error for
 681 the Felsberg algorithm increases. This flaw results from the
 682 absence in the latter of any strategy to account for large
 683 displacements, as the pyramidal refinement adopted in the
 684 Zang algorithm and the proposed algorithm.

685 Finally, Fig. 10 shows the benefits derived from the mul-
 686 tiscale window choice of Section III-B. The color display
 687 represents the scale retained in the velocity computation
 688 while the title reports the corresponding endpoint error. The
 689 progressive error reduction shows how the window selection
 690 procedure allows the computation of more consistent velocity
 691 estimates. The block-like appearance of the color maps results
 692 from the estimate stopping at scale $j = 3$, so that one velocity
 693 is computed every 2^3 pixels. A pixel-wise map is then obtained
 694 by nearest-neighbor interpolation.

695 With respect to Fig. 10, it is also interesting to note that,
 696 while the scale $j = 2$ was also considered, it was never
 697 selected in the velocity computation. This reveals that the
 698 automatic window selection procedure makes the algorithm
 699 almost independent on the chosen range $[J_f, J_c]$.

700 Again, besides being more precise, the proposed algorithm
 701 is somewhat more computationally effective than the Zang
 702 algorithm. As an example, the computation time for one A4C
 703 image (size, 271×333 pixels²) with the optimal parameters
 704 was 0.68 s while it was 18.6 s for the Zang algorithm. This
 705 point is even more important here than with MRI. Indeed,
 706 although off-line processing is considered acceptable in the
 707 latter case, it would not be for ultrasound, where the real-time
 708 aspect is one of the major attractions.

VI. CONCLUSION

710 We have described a novel algorithm for the analysis
 711 of heart motion from medical images. The displacement is
 712 estimated from the monogenic phase and is therefore robust

713 to possible variations of the local image energy. A local affine
 714 model accounts for the typical contraction, torsion and shear
 715 of myocardial fibers. An effective B-spline multiresolution
 716 strategy automatically selects the scale returning the most con-
 717 sistent velocity estimate. The multiresolution strategy together
 718 with a least-squares estimate of the monogenic orientation
 719 make the algorithm robust under image noise.

720 Due to its general formulation, the proposed algorithm is
 721 well suited for measuring myocardial motion from images
 722 from different modalities. In particular, we have presented
 723 an evaluation on cardiac tagged MRI and echocardiographic
 724 sequences. The results have shown that the proposed algorithm
 725 is a valid alternative to state-of-the-art techniques in the two
 726 fields. Moreover, it was shown to be more accurate and
 727 considerably less computation-demanding than another recent
 728 algorithm based on the monogenic signal [24].

729 A potentially valuable application is motion compensation
 730 of myocardial perfusion MRI images [7]. Indeed, the major
 731 challenge in correcting the motion problem is that the local
 732 tissue contrast in the image sequence changes locally with
 733 time, especially in the region of interest, the left ventricular
 734 myocardium. Due to the low sensitivity to alterations in the
 735 brightness profile, we believe the application of the proposed
 736 algorithm to this problem could lead to beneficial results.

APPENDIX

ZANG ALGORITHM FOR OPTICAL FLOW COMPUTATION

737 The Zang algorithm, reported in [24], is based on an
 738 extension of the monogenic signal for intrinsically 2D struc-
 739 tures, called *monogenic curvature tensor*. The motion estimate
 740 is then obtained by plugging this new feature in the popular
 741 non-linear energy function of Bruhn *et al.* [36]:
 742
 743

$$E(\mathbf{w}) = \int_{\Omega} \left(\psi_1 \left(\mathbf{w}^T J_{\rho} (\nabla_3 \varphi + \gamma \nabla_3 \Phi) \mathbf{w} \right) \right) dx dy + \alpha \int_{\Omega} \psi_2 \left(|\nabla \mathbf{w}|^2 \right) dx dy. \quad (19)$$

744 where $\mathbf{w} = [d_1, d_2, 1]$, $\nabla_3 = [\partial_x, \partial_y, \partial_t]$, $J_{\rho} (\nabla_3 f) =$
 745 $K_{\rho} * (\nabla_3 f \nabla_3 f^T)$, $\psi_i(z) = 2\beta_i \sqrt{1 + z/\beta_i}$, α , γ and β are
 746 constant parameters and K_{ρ} is a Gaussian kernel with standard
 747 deviation ρ . The two terms φ and Φ are the monogenic signal
 748 and monogenic curvature phases, respectively.
 749

750 The minimization of (19) is carried out as in [24], [36] with
 751 two nested iterative procedures. An outer fixed point cycle in
 752 ψ_1 , ψ_2 to remove the non-linearity and an inner *successive*
 753 *over-relaxation method* (SOR) to solve the resulting linear
 754 problem. A pyramidal refinement scheme is also employed,
 755 as in [24], [36].
 756

REFERENCES

- 757
 758 [1] M. Felsberg and G. Sommer, "The monogenic signal," *IEEE Trans.*
 759 *Signal Process.*, vol. 49, no. 12, pp. 3136–3144, Dec. 2001.
 760 [2] J. Noble and D. Boukerroui, "Ultrasound image segmentation: A sur-
 761 vey," *IEEE Trans. Med. Imag.*, vol. 25, no. 8, pp. 987–1010, Aug.
 762 2006.
 763 [3] C. Meyer, P. Bland, and J. Pipe, "Retrospective correction of intensity
 764 inhomogeneities in MRI," *IEEE Trans. Med. Imag.*, vol. 14, no. 1, pp.
 765 36–41, Mar. 1995.

- 766 [4] L. Axel and L. Dougherty, "MR imaging of motion with spatial
767 modulation of magnetization," *Radiology*, vol. 171, no. 3, pp. 841–845,
768 Jun. 1989.
- 769 [5] I. Smal, N. Carranza-Herrezuelo, S. Klein, W. Niessen, and E. Meijering,
770 "Quantitative comparison of tracking methods for motion analysis in
771 tagged MRI," in *Proc. IEEE Int. Symp. Biomed. Imag., Nano Macro*,
772 Apr. 2011, pp. 345–348.
- 773 [6] Z. Qian, Q. Liu, D. Metaxas, and L. Axel, "Identifying regional cardiac
774 abnormalities from myocardial strains using nontracking-based strain
775 estimation and spatio-temporal tensor analysis," *IEEE Trans. Med.
776 Imag.*, vol. 30, no. 12, pp. 2017–2029, Dec. 2011.
- 777 [7] N. M. Wilke, M. Jerosch-Herold, A. Zenovich, and A. E. Stillman,
778 "Magnetic resonance first-pass myocardial perfusion imaging: Clinical
779 validation and future applications," *J. Magn. Reson. Imag.*, vol. 10, no. 5,
780 pp. 676–685, 1999.
- 781 [8] M. Mellor and M. Brady, "Phase mutual information as a similarity
782 measure for registration," *Med. Image Anal.*, vol. 9, no. 4, pp. 330–343,
783 2005.
- 784 [9] A. Wong and J. Orchard, "Robust multimodal registration using local
785 phase-coherence representations," *J. Signal Process. Syst.*, vol. 54,
786 nos. 1–3, pp. 89–100, Jan. 2009.
- 787 [10] M. Mulet-Parada and J. Noble, "2D+T acoustic boundary detection
788 in echocardiography," *Med. Image Anal.*, vol. 4, no. 1, pp. 21–30,
789 2000.
- 790 [11] K. Rajpoot, V. Grau, and J. Noble, "Local-phase based 3D boundary
791 detection using monogenic signal and its application to real-time 3-D
792 echocardiography images," in *Proc. IEEE Int. Symp. Biomed. Imag.,
793 Nano Macro*, Jul. 2009, pp. 783–786.
- 794 [12] A. Belaïd, D. Boukerroui, Y. Maingourd, and J.-F. Lerallut, "Phase-based
795 level set segmentation of ultrasound images," *IEEE Trans. Inf. Technol.
796 Biomed.*, vol. 15, no. 1, pp. 138–147, Jan. 2011.
- 797 [13] V. Grau and J. Noble, "Adaptive multiscale ultrasound compounding
798 using phase information," in *Medical Image Computing and Computer-
799 Assisted Intervention* (Lecture Notes in Computer Science), vol. 3749,
800 Berlin, Germany: Springer-Verlag, 2005, pp. 589–596.
- 801 [14] V. Grau, H. Becher, and J. Noble, "Registration of multiview real-time
802 3-D echocardiographic sequences," *IEEE Trans. Med. Imag.*, vol. 26,
803 no. 9, pp. 1154–1165, Sep. 2007.
- 804 [15] N. Chenouard and M. Unser, "3D steerable wavelets and monogenic
805 analysis for bioimaging," in *Proc. IEEE Int. Symp. Biomed. Imag., Nano
806 Macro*, Apr. 2011, pp. 2132–2135.
- 807 [16] C. Wachinger, T. Klein, and N. Navab, "The 2D analytic signal for
808 envelope detection and feature extraction on ultrasound images," *Med.
809 Image Anal.*, vol. 16, no. 6, pp. 1073–1084, 2012.
- 810 [17] M. Sühling, C. Jansen, M. Arigovindan, P. Buser, S. Marsch, M. Unser,
811 and P. Hunziker, "Multiscale motion mapping: A novel computer vision
812 technique for quantitative, objective echocardiographic motion measure-
813 ment independent of doppler: First clinical description and validation,"
814 *Circulation*, vol. 110, no. 19, pp. 3093–3099, Nov. 2004.
- 815 [18] J. D'Hooge, A. Heimdal, F. Jamal, T. Kukulski, B. Bijnens, F. Rade-
816 makers, L. Hatle, P. Suetens, and G. R. Sutherland, "Regional strain and
817 strain rate measurements by cardiac ultrasound: Principles, implementa-
818 tion and limitations," *Eur. J. Echocardiogr.*, vol. 1, no. 3, pp. 154–170,
819 2000.
- 820 [19] M. Felsberg, "Optical flow estimation from monogenic phase," in *Proc.
821 1st Int. Conf. Complex Motion*, 2004, pp. 1–13.
- 822 [20] M. Sühling, M. Arigovindan, P. Hunziker, and M. Unser, "Multires-
823 olution moment filters: Theory and applications," *IEEE Trans. Image
824 Process.*, vol. 13, no. 4, pp. 484–495, Apr. 2004.
- 825 [21] M. Sühling, M. Arigovindan, C. Jansen, P. Hunziker, and M. Unser,
826 "Myocardial motion analysis from B-mode echocardiograms," *IEEE
827 Trans. Image Process.*, vol. 14, no. 4, pp. 525–536, Apr. 2005.
- 828 [22] M. Unser, D. Sage, and D. Van De Ville, "Multiresolution monogenic
829 signal analysis using the Riesz–Laplace wavelet transform," *IEEE Trans.
830 Image Process.*, vol. 18, no. 11, pp. 2402–2418, Nov. 2009.
- 831 [23] T. Arts, F. Prinzen, T. Delhaas, J. Milles, A. Rossi, and P. Clarysse,
832 "Mapping displacement and deformation of the heart with local sine-
833 wave modeling," *IEEE Trans. Med. Imag.*, vol. 29, no. 5, pp. 1114–1123,
834 May 2010.
- 835 [24] D. Zang, L. Wietzke, C. Schmaltz, and G. Sommer, "Dense opti-
836 cal flow estimation from the monogenic curvature tensor," in *Proc.
837 1st Int. Conf. Scale Space Variat. Methods Comput. Vis.*, 2007, pp.
838 239–250.
- 839 [25] M. Felsberg and G. Sommer, "The monogenic scale-space: A unifying
840 approach to phase-based image processing in scale-space," *J. Math.
841 Imag. Vis.*, vol. 21, no. 1, pp. 5–26, 2004.
- [26] G. Granlund and H. Knutsson, *Signal Processing for Computer Vision*.
Dordrecht, The Netherlands: Kluwer, 1995.
- [27] D. Boukerroui, J. A. Noble, and M. Brady, "On the choice of band-pass
quadrature filters," *J. Math. Imag. Vis.*, vol. 21, no. 1, pp. 53–80, 2004.
- [28] L. Wietzke and G. Sommer, "The signal multi-vector," *J. Math. Imag.
Vis.*, vol. 37, no. 2, pp. 132–150, 2010.
- [29] J. Bigun, G. Granlund, and J. Wiklund, "Multidimensional orientation
estimation with applications to texture analysis and optical flow," *IEEE
Trans. Pattern Anal. Mach. Intell.*, vol. 13, no. 8, pp. 775–790, Aug.
1991.
- [30] B. D. Lucas and T. Kanade, "An iterative image registration technique
with an application to stereo vision," in *Proc. 7th Int. Joint Conf. Artif.
Intell.*, 1981, pp. 674–679.
- [31] J. R. Bergen, P. Anandan, K. J. Hanna, and R. Hingorani, "Hierarchical
model-based motion estimation," in *Proc. 2nd Eur. Conf. Comput. Vis.*,
1992, pp. 237–252.
- [32] G. Farneback, "Very high accuracy velocity estimation using orienta-
tion tensors, parametric motion, and simultaneous segmentation of the
motion field," in *Proc. 8th IEEE Int. Conf. Comput. Vis.*, vol. 1, Mar.
2001, pp. 171–177.
- [33] M. Ledesma-Carbayo, J. Kybic, M. Desco, A. Santos, M. Sühling,
P. Hunziker, and M. Unser, "Spatio-temporal nonrigid registration for
ultrasound cardiac motion estimation," *IEEE Trans. Med. Imag.*, vol. 24,
no. 9, pp. 1113–1126, Sep. 2005.
- [34] B. K. P. Horn and B. G. Schunck, "Determining optical flow," *Artif.
Intell.*, vol. 17, nos. 1–3, pp. 185–203, Aug. 1981.
- [35] C. J. Westelius, "Focus of attention and gaze control for robot vision,"
Ph.D. dissertation, Dept. Electr. Eng., Linköping Univ., Linköping,
Sweden, 1995.
- [36] A. Bruhn, J. Weickert, and C. Schnörr, "Lucas/Kanade meets Horn-
Schunck: Combining local and global optic flow methods," *Int. J.
Comput. Vis.*, vol. 61, pp. 211–231, Feb. 2005.
- [37] M. Otte and H. Nagel, "Optical flow estimation: Advances and com-
parisons," in *Computer Vision* (Lecture Notes in Computer Science),
vol. 800, J.-O. Eklundh, Ed. Berlin, Germany: Springer-Verlag, 1994,
pp. 49–60.
- [38] S. Baker, D. Scharstein, J. P. Lewis, S. Roth, M. J. Black, and R. Szeliski,
"A database and evaluation methodology for optical flow," *Int. J.
Comput. Vis.*, vol. 92, pp. 1–31, Mar. 2011.
- [39] N. Osman, E. McVeigh, and J. Prince, "Imaging heart motion using
harmonic phase MRI," *IEEE Trans. Med. Imag.*, vol. 19, no. 3, pp.
186–202, Mar. 2000.
- [40] D. J. Fleet and A. D. Jepson, "Computation of component image velocity
from local phase information," *Int. J. Comput. Vis.*, vol. 5, no. 1, pp.
77–104, Sep. 1990.
- [41] P. Clarysse, J. Tafazzoli, P. Delachartre, and P. Croisille, "Simulation
based evaluation of cardiac motion estimation methods in tagged-MR
image sequences," *J. Cardiovasc. Magn. Reson.*, vol. 13, p. 360, Feb.
2011.
- [42] P. Clarysse, C. Basset, L. Khouas, P. Croisille, D. Friboulet, C. Odet,
and I. Magnin, "2D spatial and temporal displacement field fitting from
cardiac MR tagging," *Med. Image Anal.*, vol. 3, pp. 253–268, Aug.
2000.
- [43] W. Daniel, *Applied Nonparametric Statistics*. Belmont, CA: Duxbury
Thomson Learning, 2000.
- [44] V. Chalana and Y. Kim, "A methodology for evaluation of boundary
detection algorithms on medical images," *IEEE Trans. Med. Imag.*,
vol. 16, no. 5, pp. 642–652, Oct. 1997.
- [45] B. Galvin, B. Mccane, K. Novins, D. Mason, and S. Mills, "Recovering
motion fields: An evaluation of eight optical flow algorithms," in *Proc.
British Mach. Vis. Conf.*, 1998, pp. 195–204.
- [46] T. L. Szabo, *Diagnostic Ultrasound Imaging: Inside Out*. Burlington,
MA: Elsevier, 2004.
- [47] G. R. Sutherland, G. D. Salvo, P. Claus, J. D'Hooge, and B. Bijnens,
"Strain and strain rate imaging: A new clinical approach to quantifying
regional myocardial function," *J. Amer. Soc. Echocardiogr.*, vol. 17,
no. 7, pp. 788–802, 2004.
- [48] T. Marwick, M. Yu, and J. Sun, *Myocardial Imaging: Tissue Doppler
and Speckle Tracking*. Oxford, U.K.: Blackwell, 2007.
- [49] J. Kybic and M. Unser, "Fast parametric elastic image registration,"
IEEE Trans. Image Process., vol. 12, no. 11, pp. 1427–1442, Nov.
2003.
- [50] T. Maltaverne, P. Delachartre, and A. Basarab, "Motion estimation using
the monogenic signal applied to ultrasound elastography," in *Proc. Annu.
Int. Conf. Eng. Med. Biol. Soc.*, Sep. 2010, pp. 33–36.

- 917 [51] M. Alessandrini, H. Liebgott, D. Friboulet, and O. Bernard, "Simulation
918 of realistic echocardiographic sequences for ground truth validation of
919 motion estimation," in *Proc. IEEE Int. Conf. Image Process.*, Orlando,
920 FL, 2012, pp. 2329–2332.
- 921 [52] T. Dietenbeck, M. Alessandrini, D. Barbosa, J. D'Hooge, D. Fri-
922 boulet, and O. Bernard, "Detection of the whole myocardium in 2D-
923 echocardiography for multiple orientations using a geometrically con-
924 strained level-set," *Med. Image Anal.*, vol. 16, no. 2, pp. 386–401,
925 2012.



926 **Martino Alessandrini** received the M.Sc. degree
927 in electronic engineering from the University of
928 Bologna, Bologna, Italy, and the Ph.D. degree from
929 the Advanced Research Center on Electronic Sys-
930 tems for Information and Communication Technolo-
931 gies, Ercole De Castro, Bologna, in 2007 and 2011,
932 respectively.

933 He is currently a Post-Doctoral Researcher with
934 the Centre de Recherché en Imagerie Médicale
935 (CREATIS), Lyon, France. His current research
936 interests include processing of medical ultrasound
937 images, with a focus on image restoration, registration, segmentation, despeck-
938 ling, tissue characterization, and motion tracking techniques.

939 Dr. Alessandrini was a recipient of the Post-Doctoral Research Grant from
940 CREATIS.



941 **Adrian Basarab** received the M.S. and Ph.D.
942 degrees in signal and image processing from the
943 National Institute for Applied Sciences of Lyon,
944 Lyon, France, in 2005 and 2008, respectively.

945 He has been an Associate Professor with the
946 Université Toulouse III—Paul Sabatier, Toulouse,
947 France, and a member of the Institut de Recherche
948 en Informatique de Toulouse Laboratory (UMR
949 CNRS 5505), Toulouse, since 2009. His current
950 research interests include medical imaging with a
951 focus on motion estimation, inverse problems, and
952 ultrasound image formation.



953 **Hervé Liebgott** received the Master's degree in
954 electrical engineering and the Master's degree in
955 acoustics from the Lyon National Institute of
956 Applied Sciences, Lyon, France in 2002, and the
957 Ph.D. degree with research on transverse oscillations
958 techniques adapted to elastography in 2005. His
959 Ph.D. research involved a six-month visit with the
960 Technical University of Denmark, Kongens Lyngby,
961 Denmark. He received the French Habilitation to
962 Lead Research (HDR) degree from University Lyon
963 1, Lyon, in 2011.

964 He is currently an Associate Professor with the Department of Electrical
965 Engineering, University Institute of Technology Lyon 1, Lyon, France, where
966 he is involved in research with a focus on image formation techniques
967 and motion estimation. He is currently the Vice Leader of the Ultrasound
968 Imaging Team, Centre de Recherché en Imagerie Médicale, Lyon, France.
969 He is currently involved in three main research projects: 1) needle biopsy
970 guidance in 3-D ultrasound using matrix arrays; 2) transverse oscillation
971 techniques adapted to echocardiography (the U.S.-Tagging project for which
972 he received a Young Researcher Grant from the French National Research
973 Agency); and 3) application of compressed sensing to medical ultrasound.
974 He conducts research on the processing of medical ultrasound images, with
975 a focus on image restoration, registration, segmentation, despeckling, tissue
976 characterization, and motion tracking techniques. His current research interests
977 include image and signal processing applied to medical ultrasound imaging.



978 **Olivier Bernard** received the B.S. and Ph.D.
979 degrees in electrical engineering from the National
980 Institute for Applied Sciences of Lyon (INSA-Lyon),
981 Villeurbanne, France, in 2003 and 2006, respec-
982 tively.

983 He was a Post-Doctoral Research Fellow with
984 the Biomedical Imaging Group, École Polytechnique
985 Fédérale de Lausanne, Lausanne, Switzerland, in
986 2007. He became an Associate Professor with INSA-
987 Lyon and a member of the CREATIS Laboratory
988 (CNRS 5220, INSERM U1044, INSA-Lyon, Univer-
989 sity of Lyon), Lyon, France, in 2007. His current research interests include
990 biomedical signal and image processing, particularly image segmentation,
991 motion estimation, statistical modeling, and sampling theories.

992 Dr. Bernard was a recipient of the Special Mention (Second Prize) for
993 the best Ph.D. thesis in France from the IEEE Engineering in Medicine and
994 Biology Society in 2008.

AUTHOR QUERY

AQ:1 = Please confirm the volume no for ref. [13].

IEEE
Proof